ELSEVIER

Contents lists available at ScienceDirect

International Journal of Refractory Metals and Hard Materials

journal homepage: www.elsevier.com/locate/IJRMHM





Investigation of microstructures, defects, and mechanical properties of titanium-zirconium-molybdenum alloy manufactured by wire arc additive manufacturing

Saiful Islam ^a, Gi-Jeong Seo ^b, Md.R.U. Ahsan ^a, Herminso Villarraga-Gómez ^c, Ho-Jin Lee ^d, Duck Bong Kim ^{b, *}

- ^a Department of Mechanical Engineering, Tennessee Technological University, Cookeville, TN 38505, United States
- b Department of Manufacturing and Engineering Technology, Tennessee Technological University, Cookeville, TN 38505, United States
- ^c X-ray Quality Solutions Manager, ZEISS Industrial Quality Solutions, Carl Zeiss Industrial Metrology, LLC, MI 48116, United States
- d Extreme Fabrication Technology Group, Korea Institute of Industrial Technology, 350-27, Gumi-daero, Gumi-si, Gyeongsang buk-do 39253, Republic of Korea

ARTICLE INFO

Keywords:

Titanium-zirconium-molybdenum (TZM) Wire arc additive manufacturing (WAAM) Microstructure Mechanical properties Porosity

ABSTRACT

Titanium-zirconium-molybdenum (TZM), one of the refractory alloys, has extraordinary physicochemical properties, making it ideal for usage in extreme environmental applications (e.g., high-temperature and nuclear). Due to the scalability and near-net shape fabrication, metal additive manufacturing processes have several advantages, leading it to be the possible solution for the fabrication of refractory alloy structures. Wire arc additive manufacturing (WAAM) has several advantages, including high deposition rate, energy efficiency, and cost-effective manufacturing of large components. In this study, we comprehensively investigated the relationships among process, microstructures, mechanical properties, and defects of TZM thin-walls manufactured by WAAM using four heat input conditions: 180A, 200A, 220A, and 240A. The microstructures were investigated using multi-scale material characterization techniques. Columnar grains were generated along the build direction, and carbide precipitates were found uniformly distributed in the Mo matrix. Multi-scale pores and cracks were present in the microstructures. The average microhardness values for the deposits ranged from 188.5 to 193.5 hardness scales of Vickers. The highest yield strength, 195 MPa, was found in the 200A heat input condition. The primary fracture mode was identified as a brittle transgranular. The area fraction of porosity was calculated >1% in each condition, with the largest being 2.04% in the 240A deposit.

1. Introduction

Molybdenum (Mo) is a refractory element which is characterized by a high melting point (2623 °C), a low coefficient of thermal expansion (4.8 μ m/m·K at 25 °C), high electrical and thermal conductivities (138 W/m·K), as well as high corrosion and creep resistance [1–3]. Due to these extraordinary physicochemical properties and high strength at elevated temperatures, Mo has a wide range of potential areas for extreme environment applications, including aerospace, nuclear, power generation, and chemical and electronics industries [4]. But, lower recrystallization temperature (1100 °C) compared to the melting point and the high ductile-to-brittle transition temperature (DBTT) greatly inhibit its applications [5,6]. To over the limitations, Mo-based alloys are preferred over pure Mo. Titanium-zirconium-molybdenum (TZM) is

one of the most widely used Mo-based alloys, which has the composition of 0.5 wt% titanium (Ti), 0.08 wt% zirconium (Zr), and 0.02 wt% carbon (C) [7]. Due to Ti, Zr, and C, carbide particles are precipitated and dispersed homogeneously in the Mo matrix and grain boundaries. Carbides at grain boundaries inhibit grain growth, thus increasing the thermal energy required for recrystallization [5,8]. Consequently, recrystallization temperature is increased to 1400 °C, which improves creep resistance and mechanical properties [9–12]. Due to these unique characteristics, TZM has the potential for high-temperature applications, compared to traditional superalloys [13].

Typically, TZM is manufactured by vacuum arc melting or powder metallurgy (PM) [14]. Although PM is widely used due to the consistency of alloy composition, homogeneity, and better phase distribution, it has several limitations regarding the production of parts with near-

E-mail address: dkim@tntech.edu (D.B. Kim).

^{*} Corresponding author.

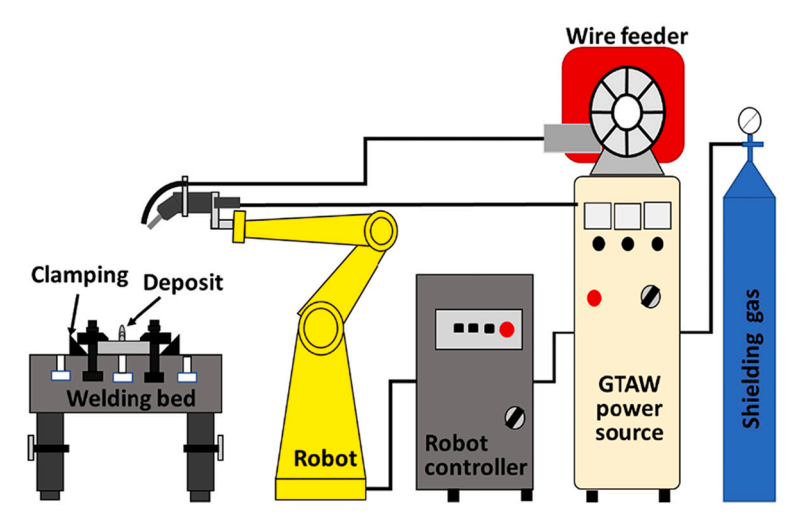


Fig. 1. Schematic diagram of GTA-WAAM system.

net-shape and complex geometry. Furthermore, PM products are mostly semi-finished and must be machined to attain the final shape. TZM is an expensive and hard-to-machine material, resulting in additional cost and time for the post-processing [4]. To overcome these issues, metal additive manufacturing (AM) processes have been investigated to fabricate the TZM structures. AM creates parts by depositing material in a layer-by-layer stacking mechanism. This unique feature enables the manufacturing of complex or customized parts from the design, eliminating the requirement of machining for the final component. A significant reduction in the part count can be also realized by eliminating or reducing the need to assemble multiple components [15]. In addition, it can reduce production cost by minimizing material waste (lower buy to fly ratio) and deposition time compared to subtractive machining processes [16,17].

According to American Society for Testing and Materials (ASTM) standard terminology, single-step metal AM techniques are classified as (1) powder bed fusion (PBF), (2) directed energy deposition (DED), and (3) sheet lamination [18]. DED techniques can be classified as powderfed and wire-fed systems based on the feedstock used. The powder-fed system is suitable for creating a part with excellent geometric accuracy, but its deposition rate is slow (10 g/min). Wire + arc additive manufacturing (WAAM) is a DED technology using a wire feedstock and a welding arc energy source [19,20]. It has several advantages, including an inexpensive system setup and a high deposition rate. In addition, it has a higher energy efficiency of 90% [21], compared to the 2–5% of a laser and 15–20% of an electron beam, respectively [16]. The low cost and the high energy efficiency coupled with ease of operation and wide availability of wire feedstocks make the WAAM process ideal for small- and medium-sized enterprises. It can be classified into three categories: gas tungsten arc (GTA), gas metal arc (GMA), and plasma arc (PA) [22]. Due to the high thermal diffusivity of TZM, heat is dissipated at a high rate during the deposition process. Thus, high-intensity heat source, such as GTA, is preferred for the welding of TZM [23].

Defects in WAAM can be generated by various factors, including unstable weld pool dynamics, heat accumulation, and environmental effects (e.g., gas contamination) [24]. Due to the high-intensity electric arc heat source, WAAM parts undergo repeated melting and cooling cycles during the deposition process, resulting in the heat accumulation in the workpiece as new layers are deposited. This affects the cooling rate, and large thermal gradients are developed in the part. The non-equilibrium thermal cycles and large thermal gradients generate residual stress, heterogeneous microstructures, and defects after the process. Residual stress leads to dimensional inaccuracy, part distortion, and cracks, while the microstructural heterogeneity induces anisotropic material properties. Porosity, which is generated due to the formation of

oxides in the presence of oxygen, can also lead to poor properties [25]. These issues are more magnified when AM is used to fabricate the refractory alloy structures due to the extraordinary thermomechanical and unique properties, resulting in deteriorated mechanical properties.

Several studies have been carried out on the manufacturing and joining of Mo and TZM alloy components. Researchers have investigated different arc melting and PM methods to manufacture TZM. Chakraborty and Krishnamurthy used a non-consumable arc melting process to manufacture the alloys [10], and Hu et al. [6] utilized PM to prepare lanthanum-doped TZM alloy plates. Strength and elongation increased due to doping La into the TZM all. The nanostructured temperatureresistant TZM alloy was synthesized using mechanical milling followed by sintering in Ahmadi et al. [26]. Danisman et al. [7] studied the effect of sintering conditions on densification, microstructure, and hardness of pre-alloyed TZM powder. Ghazali et al. [12] studied mechanical behavior and microstructural analysis of TZM alloy produced by a metal injection molding (MIM) method at different annealing temperatures. Wei et al. [27] manufactured carbon nanotubes reinforced TZM composite utilizing high energy ball milling and spark plasma sintering. The changes in the microstructure of the composite powders induced by ball milling improved the relative density, hardness, and yield strength.

Researchers have reported several studies on AM of pure and alloyed Mo. Faidel et al. [28] studied the feasibility of the selective laser melting (SLM) process with pure Mo powder. They reported that using Mo powder in the SLM process is feasible, but a maximum density of 82.5%was achieved. Kaserer et al. [2] manufactured crack-free Mo parts using SLM, which achieved a maximum density of 97.7%, and alloyed Mo reached a maximum density of 99.6%. Higashi and Ozaki fabricated pure Mo samples using SLM and studied the effect of process parameters on porosity through microstructural observations [29]. Braun et al. [30] investigated the SLM technique to fabricate molybdenum and tungsten. The study identified the impact of the oxygen content of the powder, process atmosphere, and substrate temperature on the mechanical properties of the processed material. They also manufactured Mo alloyed with Carbon (Mo-0.45 wt% C) using Laser Powder Bed Fusion (LPBF) [31]. Wang et al. [32] manufactured Mo rods consisting of columnar grains by a WAAM process, and porosity was quantitatively analyzed using high-resolution computed tomography.

There have been numerous investigations on the welding of TZM alloy. Chen et al. [33] studied electron beam welding (EBW) of Mo and found tensile strength of 280 MPa in the welded joint. Zhang et al. [34] investigated the effect of Rhenium (Re) during EBW of TZM alloy. When the Re content in the weld zone reached 48.7 wt%, the tensile strength of the joint increased to 524 MPa. During laser welding of 0.5 mm-thick

Table 1
Elemental Composition (wt%) of TZM wire used in this study.

Alloying elements	Мо	Ti	Zr	С	О	N	Fe	Ni	Si
Composition (wt%)	Balance	0.40-0.55	0.06-0.12	0.01-0.04	< 0.03	< 0.002	< 0.01	< 0.005	< 0.005

Table 2
Constant process parameters.

Process Parameters	Value (unit)		
Electrode-to-workpiece distance	5 (mm)		
TZM alloy wire diameter	1 (mm)		
Tungsten electrode tip angle	45 (deg.)		
Torch angle	90 (deg.)		
Diameter of the electrode	4 (mm)		
Torch shielding gas composition	70% Ar, 30% He		
Shielding gas flow rate	14.16 (L min-1)		
Substrate	TZM		

Table 3Process parameters used for depositing four thin-walls.

Condition	TS (mm/ min)	Current (A)	WFS (mm/ min)	Energy density (J/ mm3)	Heat input (J/mm)
1	200	180	1500	138	810
2	200	200	1500	153	900
3	200	220	1500	168	990
4	200	240	1500	183	1080

TZM plate, the tensile strength of welded joint achieved 60% of the base metal. It was concluded that porosity and embrittlement were responsible for the reduced strength and ductility of the welded joint [1]. Wang et al. [35] analyzed the influence of welding current on weld quality of TZM alloy using the GTA welding process. It was found that the tensile strength and elongation of the welded specimens were much lower than the parent metal. In Chatterjee et al. [23], two systems setups, such as electron beam and laser-GTA hybrid power sources, were used to weld TZM plates in a square-butt arrangement. Weld joints had yield strength of 40% of parent metal with non-measurable tensile ductility. The failure mode mainly was transgranular brittle fracture with the presence of sharp cleavage planes and multiple slip lines.

Although WAAM has great a potential for manufacturing refractory alloy, there has been not much study on this. Thus, the knowledge about the identification of near-optimal process parameters and the relationships among process conditions, microstructures, defects, and mechanical properties is significantly lacking. This paper comprehensively investigated the microstructures, mechanical properties, and corresponding defects of wire + arc additively manufactured thin-wall TZM structures. For this, four thin-walls with different heat input conditions were deposited using the GTA-based WAAM process. Microstructures were characterized using optical and electron microscopy, elemental mapping, and X-ray diffraction. Microhardness, tensile test, and fracture surface analysis were performed to understand the mechanical properties and deformation behaviors of the structures. Porosity, which was

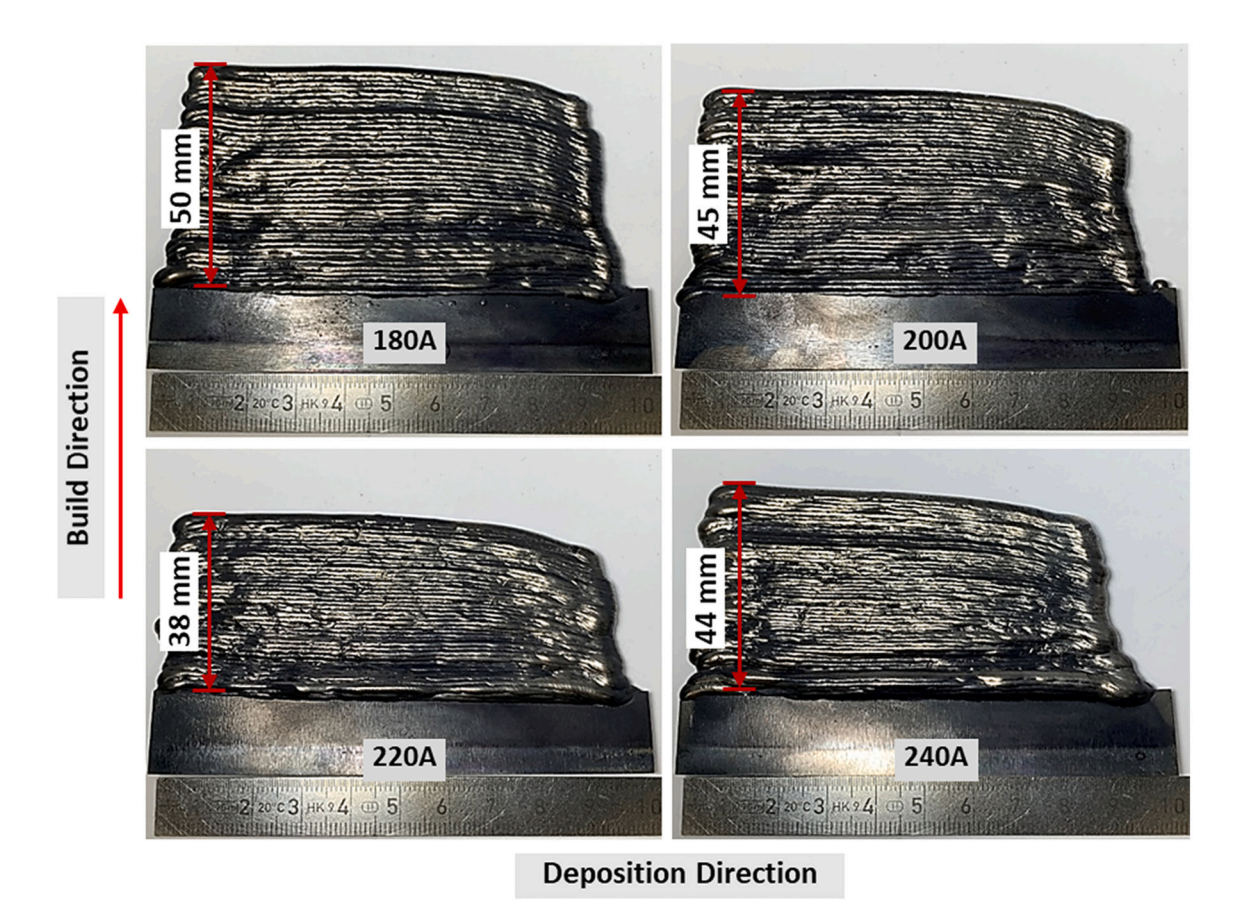


Fig. 2. Multi-layer thin-walled deposits with different heat input conditions.

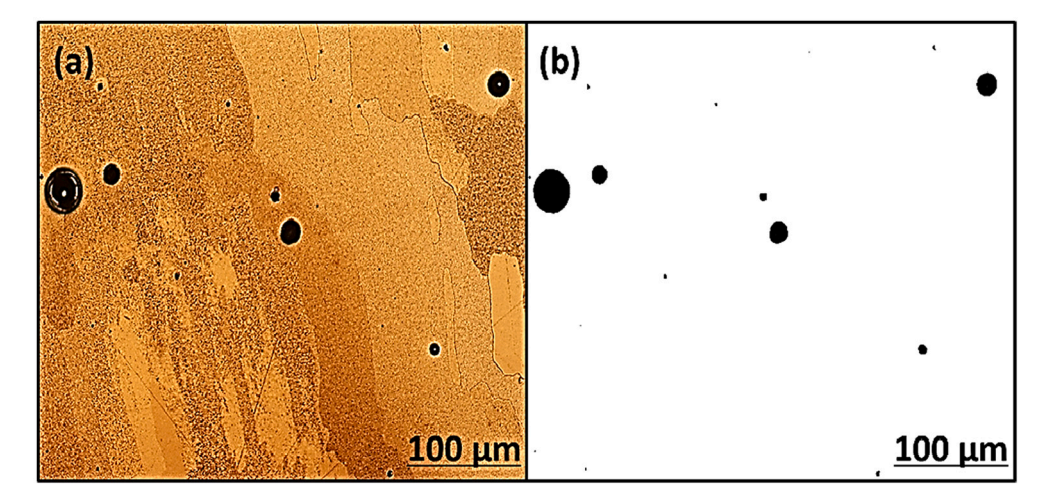


Fig. 3. (a) OM image and (b) its corresponding binary processes image generated using ImageJ.

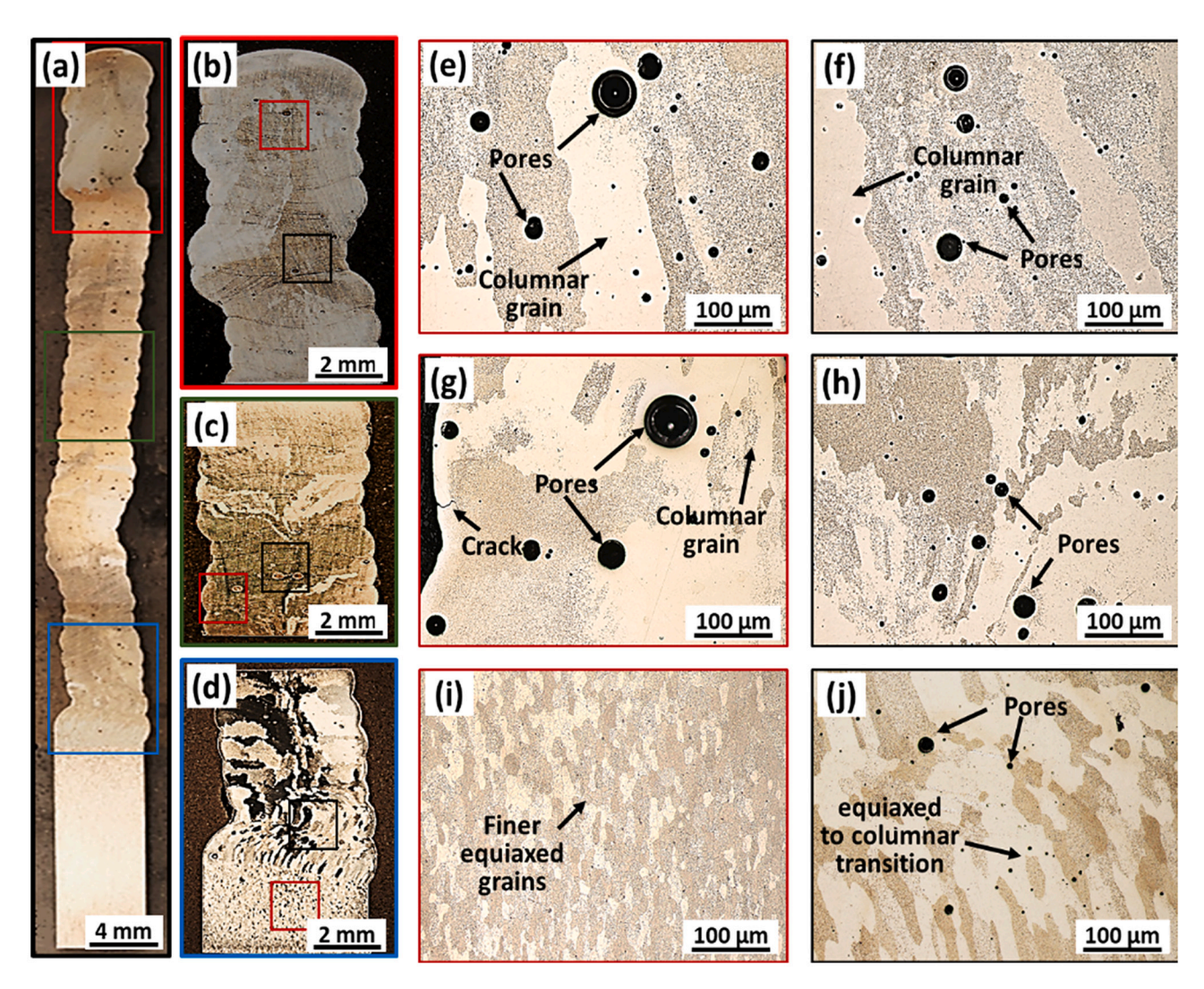


Fig. 4. Optical Microscopy images showing the microstructure of 180A WAAM-TZM deposit: (a) overall cross-section, (b-d) higher magnification images at top, middle, and bottom region, (e-j) red and black marked region of top, middle, and bottom part showing at higher magnification. (For interpretation of the references to colour in this figure legend, the reader is referred to the web version of this article.)

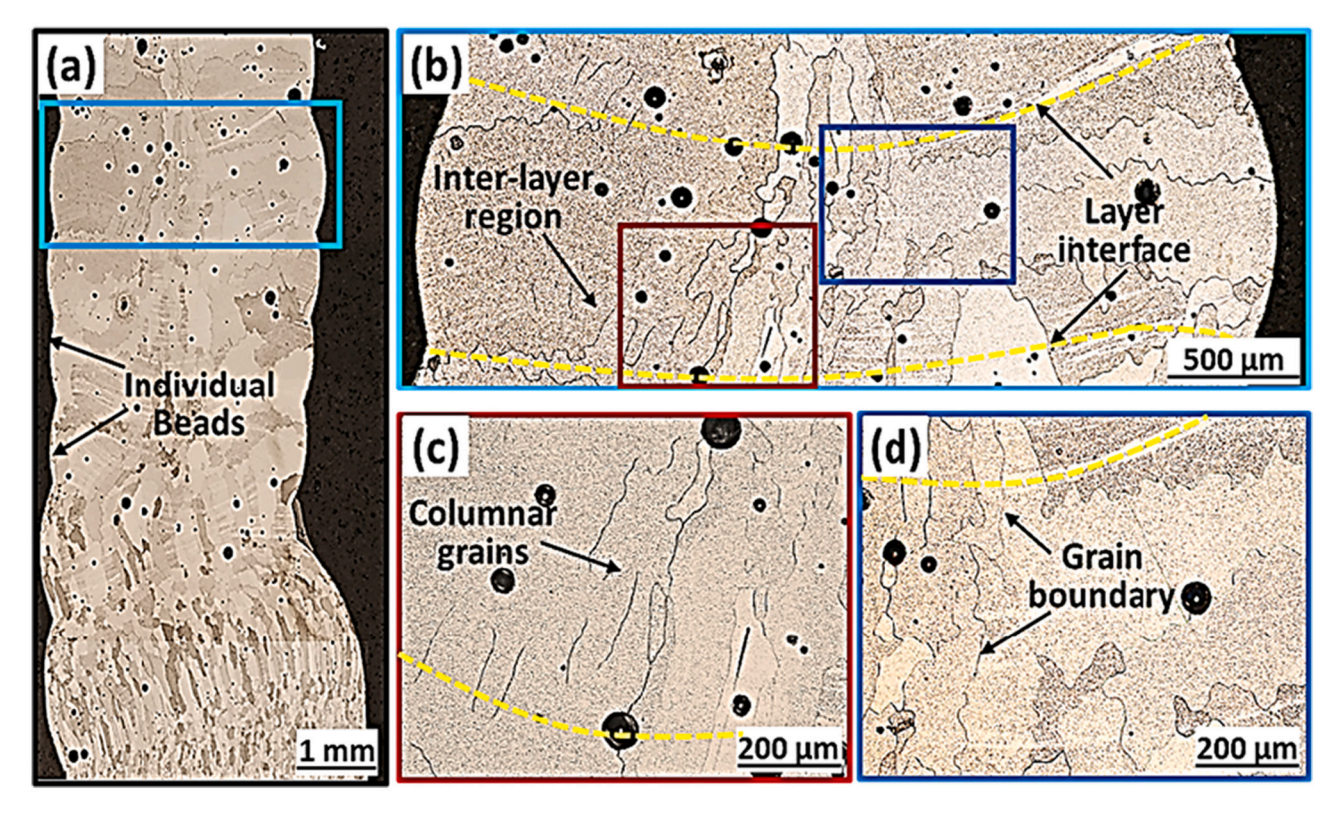


Fig. 5. OM images showing microstructure of WAAM TZM deposit: (a) bottom of the 180A condition, (b-d) showing layer interphase and interlayer region at different magnification.

identified as the major defect, had been also analyzed.

2. Material and methods

2.1. Thin-wall deposition

Figure 1 shows an schematic diagram of GTA-WAAM system used in conducting all the experiments [36]. It consists of a 6-axis Fanuc Arc-Mate 120iC robot arm with a Fanuc R-J3iB controller, a Miller Dynasty 400 GTA welding power source, and a generic wire feeder. The wire feed speed (WFS), travel speed (TS), and welding current are individually controlled through the wire feeder, robot, and power source, respectively. TZM alloy wire and substrate (ASTM B387 Type 364) were collected and used for deposition purposes, as the chemical composition is summarized in Table 1. Process parameters that were kept constant during the deposition are summarized in Table 2. Since the welding voltage depends on the distance between the electrode tip and the workpiece, all experiments were carried out with a constant gap of 5 mm to maintain consistency, as an example.

To deposit thin-walls, three factors (i.e., Current, TS, and WFS) were taken into consideration. Then, thin-walls with different heat input and energy density conditions were deposited as summarized in Table 3. TS and WFS were kept constant, while the arc current was changed. Energy density and heat input are calculated using the following Eqs. [36].

Heat input
$$(J/mm) = \frac{Current \times Voltage \times 60}{TS}$$
 (1)

Energy density
$$(J/mm^3) = \frac{Current \times Voltage \times 60}{\pi \times (wire \ radius)^2 \times WFS}$$
 (2)

Deposit conditions 1–3 consist of 40 layers, while condition 4 has 50 layers. Additional 10 layers in condition 4 were deposited to increase the height of the wall, since the height of 40 layers is insufficient to fabricate tensile test specimens. With the increase of heat input, the temperature

of the molten metal rises, and accordingly surface tension and viscosity drop. This enables the molten material to spread out more and results in the decrease of bead height [36]. Due to this, the wall height was highest at the 180A and lowest at the 240A with the 40 layers. The length of the thin-walls was kept constant at 100 mm in each condition. An argon-helium mixture was used as a shielding gas because it induced higher arc energy and heat input than pure argon gas [37]. After the deposition of each layer, the top surface was allowed to cool down to 300 $^{\circ}\text{C}$ which is measured by a handheld device with a type K thermocouple. Fig. 2 shows the four thin-walled deposits with the different heat input conditions.

2.2. Sample preparation and analysis

To study the microstructural features and microhardness of the WAAM-TZM, specimens were first cut using the metallurgical saw from the middle of the deposits. Then the surfaces of the samples were grounded using SiC abrasives (grit sizes of 240–1200) and polished using diamond paste solutions of 3 and 1 μm size. Etching was performed using Murakami's reagent (10 g KOH, 10 g K₃Fe(CN)₆, and 100 mL H₂O). For the optical microscopy (OM), a Nikon SMZ 1500 microscope was used for the low-magnification images (up to 50× magnification), and a Nikon Epiphot inverted microscope was employed for the higher magnification images. FEI Quanta 200 and Hitachi SU 7000 scanning electron microscope (SEM), equipped with an energy-dispersive X-ray spectroscope (EDS), were used for the microstructure, chemical composition, and fracture surface analyses. Rigaku Ultima IV machine was employed for the X-ray diffraction (XRD) analysis.

Microhardness tests were performed along the build direction of the polished specimens at 0.5 mm intervals from bottom to top of the deposit using a load of 500 g (Vickers diamond indenter) and a dwell time of 10s. Buehler Wilson VH1202 microhardness tester machine equipped with an integrated high-resolution camera and DiametTM software was used for the test. Mechanical strength was investigated using the

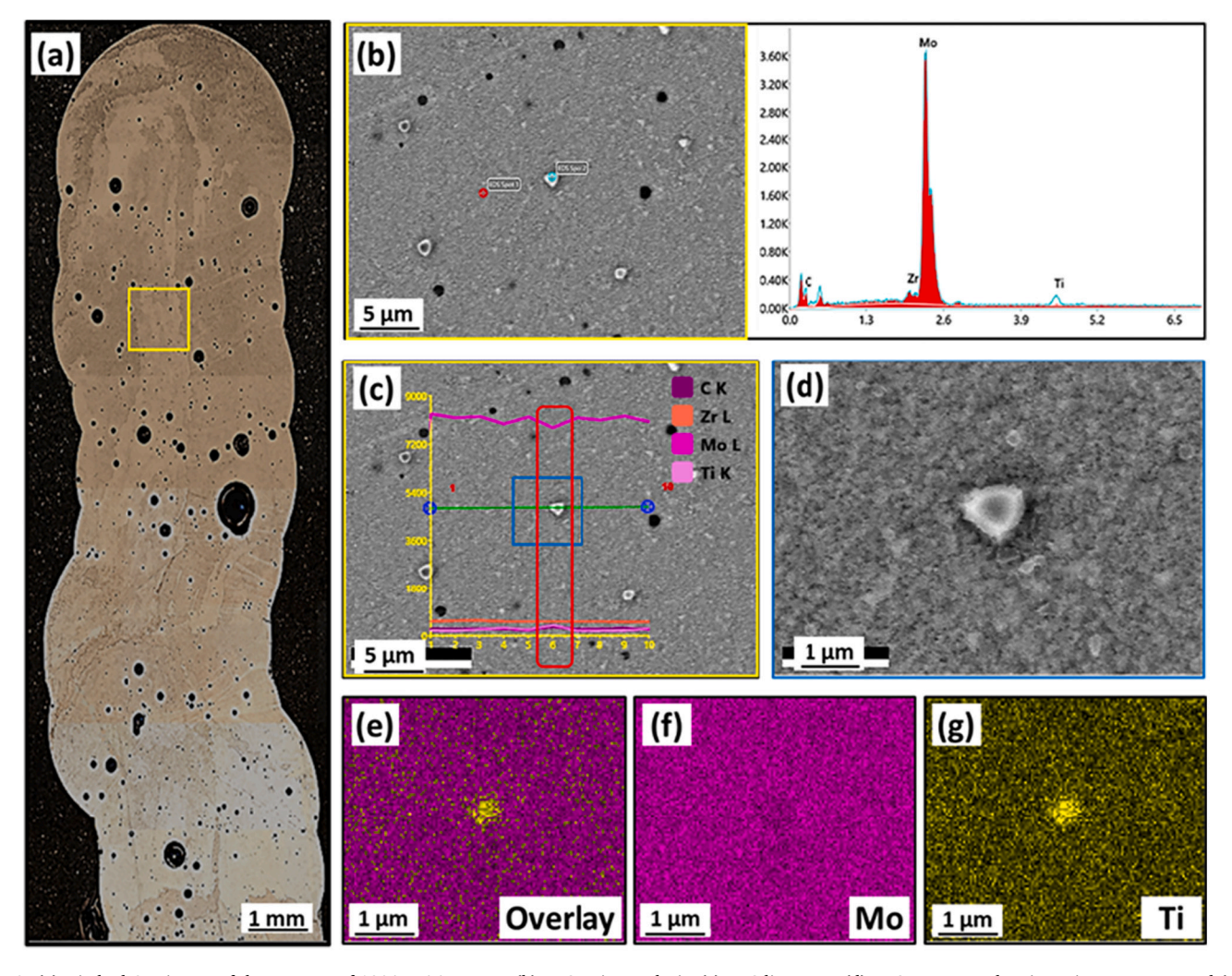


Fig. 6. (a) stitched OM image of the top part of 180A WAAM-TZM, (b) EDS point analysis, (c) EDS line scan, (d) EDS area map showing microstructure, and (e-g) corresponding elemental distribution at the top region of 180A sample.

computer-controlled, uniaxial tensile testing system (TestResources 810 E4 Electrodynamic Test Machine). The flat dog-bone-shaped specimens were prepared along the build direction from the deposited wall using wire electrical discharge machining according to the dimensions specified in the American Society for Testing and Materials (ASTM) E8 standard [38]. Tensile samples from each condition were tested at room temperature with an elongation rate of 0.1 mm/min. Before the tensile test, the samples were polished to a grit size of 600 to remove any stress concentrations from machining. The fractured locations and surfaces were analyzed using the SEM to identify the failure characteristics and evaluate the presence of anomalies.

2.3. Porosity analysis

For porosity measurement, the cross-sectional area of the deposits was polished such that only pores could be detected. The pores were then observed using the OM with manual exposure. In each heat input condition, OM images were taken from bottom to top of the deposit covering the whole cross-sectional area. A total of 30 OM images were taken across the cross-sectional area in each deposit. The images were then converted to the binary image with the constant threshold using the ImageJ software [39], as shown in Fig. 3. These binary images were then analyzed using the same software to calculate individual pore diameter and area fraction.

3. Results

3.1. Microstructure characterization

Figure 4(a) shows the optical microscopy (OM) image of the overall cross-section of the 180A deposit. Fig. 4(b)-(d) show the top, middle, and bottom parts of the deposit at higher magnification. Large columnar grains and pores are observed in the microstructure. The microstructural features of the middle and top part of the deposit marked in red and black are shown at higher magnification in Fig. 4(e)-(h). In both cases, multi-scale pore and epitaxial columnar grains are observed. In addition, the red marked region in Fig. 4(g) shows the presence of a small crack in the structure. The microstructure of the bottom part of the deposit is shown at higher magnification in Fig. 4(i) and (j). The red marked area shows the microstructure of the PM-TZM substrate which contains fine equiaxed grains, a common characteristic of PM components. The black marked regions show the equiaxed to the columnar transition of the grains. The thermal gradient developed due to directional heat flow along the build direction is responsible for this transition [12,36]. Similar microstructural features are also found in 200A, 220A, and 240A deposits. The formation of columnar grain is a common microstructural characteristic of the WAAM process [40]. Columnar grain growth occurs due to the repeated melting of the deposited layers resulting in a larger temperature gradient inside the melt pool, inhibiting nucleation of new grains during solidification [41].

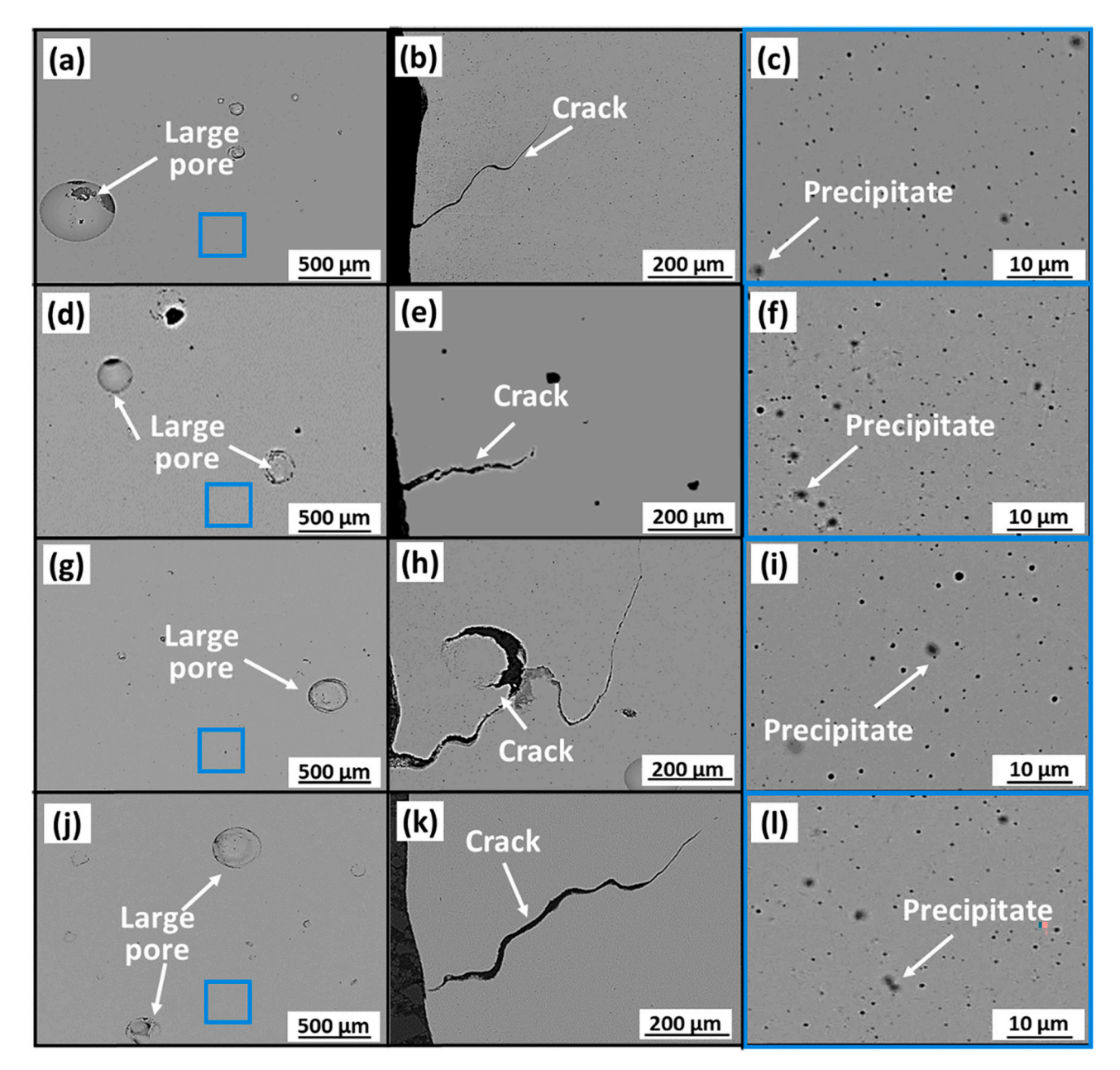


Fig. 7. SEM images showing pore, cracks, and carbide precipitates of WAAM-TZM deposits: (a-c) 180A, (d-f) 200A, (g-i) 220A, and (j-l) 240A.

Fig. 5(a) shows the overall microstructure of the bottom part of the 180A condition. Individual layers can be easily identified from the image. The Blue marked region shows the microstructure of individual layer at higher magnification in Fig. 5(b). The yellow dotted lines mark the layer interface between two layers. There has not been any significant difference in the microstructure among layer interface and interlayer regions. Elongated grains are grown across multiple layers without the presence of any other phases. Fig. 5(c)-(d) shows the regions at more high magnification which also shows a similar morphological structure. However, no cracks are evident at the layer interface or the interlayer region.

Elemental mapping was carried out on WAAM-TZM deposits to evaluate the distribution and morphology of carbide precipitates. Fig. 6 (a) shows the stitched OM images of the top region of the 180A deposit. Fig. 6(b) shows EDS point analysis spectra at two locations marked by red and blue spots. The red marked spot is located at the matrix, and the blue one is located in the grey irregular-shaped area. Comparing the elemental distribution spectra at two locations shows a larger peak

intensity of C and Ti in the blue region. This confirms that grey irregular-shaped areas in Mo matrix are carbide precipitates, mainly TiC. EDS line scan analysis is performed to investigate further, and the result is shown in Fig. 6(c). There is a drop in the Mo peak and a rise in the peak for Ti and C when the line passes through the grey area, as shown in the red zone. The peak intensity of Zr remains constant through the line scan. This confirms the presence of TiC and the absence of ZrC precipitates in the structure. EDS area mapping was performed in the blue marked area. Fig. 6(d)-(g) shows the SEM image and result of EDS area map analysis. From the overlay image, it can be seen that the microstructure consists of mainly Mo matrix. In addition, there is presence of Ti in the grey area as shown in Fig. 6(g). It also verifies that the grey irregular area is TiC and these precipitates are distributed throughout the Mo matrix.

SEM images in Fig. 7 show the microstructural features of WAAM-TZM deposits. TZM is a single-phase BCC material where different carbide particles are uniformly distributed in the Mo matrix [7]. SEM images show that WAAM-TZM also consists of a single-phase Mo matrix. Fig. 7(a)-(c) shows microstructural features of the 180A deposits. Pores

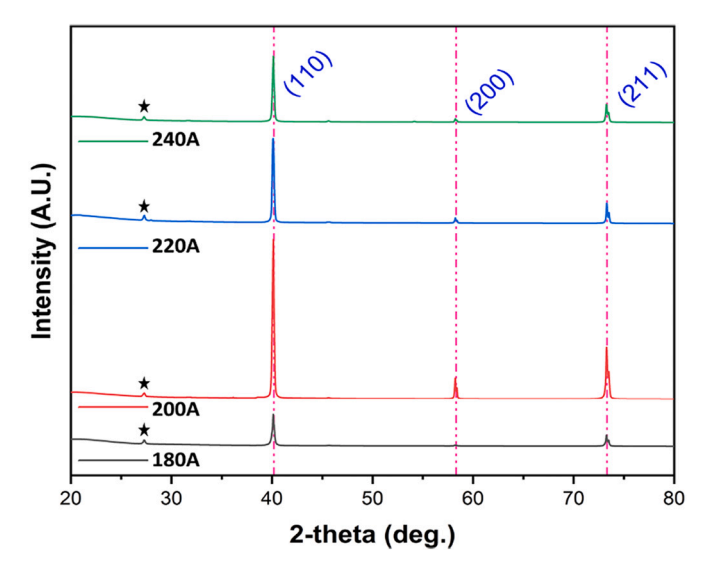


Fig. 8. X-ray diffraction pattern of the WAAM-TZM Specimens.

and cracks are present in the microstructures, as shown in Fig. 7(a) and (b). Cracks originate from the side of the deposited wall and propagate inside the structure. These are characterized as solidification cracks and depend on the solidification nature of the material [42]. A higher magnified image of the Mo matrix in Fig. 7(c) shows that grey and irregularly shaped particles (carbides) and micropores (black and circular shaped area) are distributed homogenously in the structure. Fig. 7 (d)-(l) shows microstructural characteristics of the 200A, 220A, and 240A deposits. Pores, microcracks, and carbide precipitates are observed in each case. The presence of defects can deteriorate mechanical property. Porosity is one of the common defects found in the WAAM structure of refractory elements [43]. Molybdenum oxides are volatile above 700°, and these oxides contribute to pore formation. Detailed porosity investigation is performed in Section 3.3.

Figure 8 shows the XRD pattern of the four WAAM-TZM deposits, which is carried out for scan range of $2\theta=20^\circ$ - 80° with a step width of 0.02°. Major peaks of the 180A are identified at three locations $2\theta=40.127^\circ$, 58.238° , and 73.266° , while those of the 200A are at $2\theta=40.076^\circ$, 58.246° , and 73.306° , respectively. Major peaks of the 220A are located at $2\theta=40.115^\circ$, 58.230° , and 73.282° . In the 240A, the peaks are at the location of $2\theta=40.112^\circ$, 58.228° , and 73.274° , respectively. For all the samples, the XRD pattern shows three major

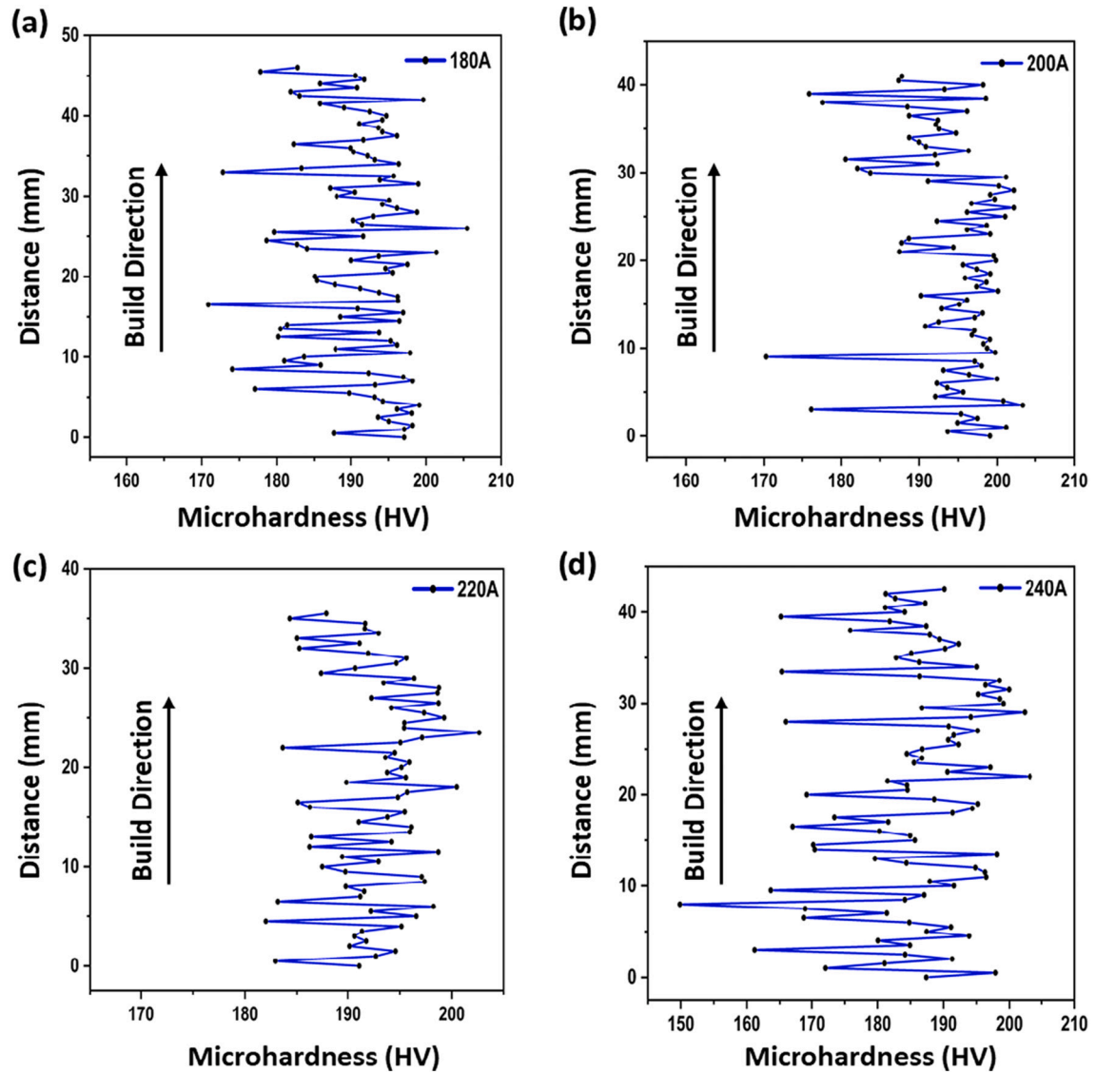


Fig. 9. Microhardness from substrate to top of the WAAM-TZM deposit: (a) 180A, (b) 200A, (c) 220A, and (d) 240A.

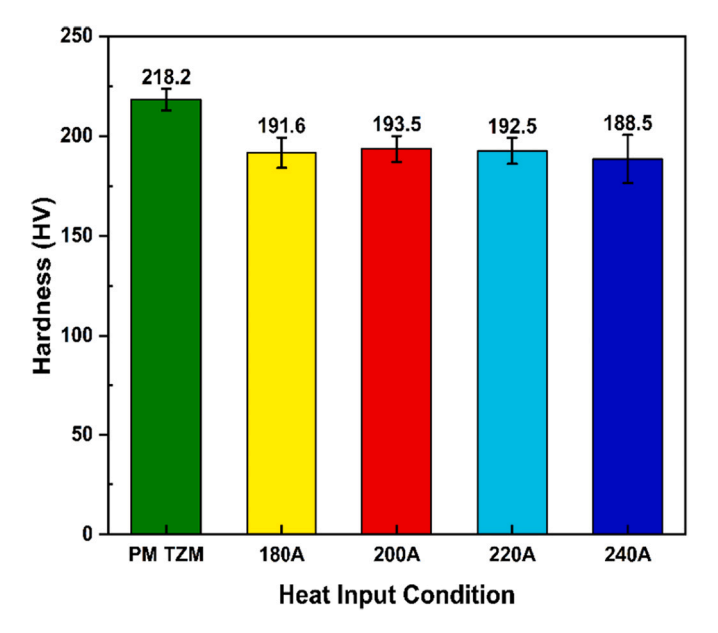


Fig. 10. Comparison of average micro-hardness among PM-TZM and WAAM-TZM with the different heat input conditions.

peaks at $2\theta \sim 40^\circ$, 58° , and 73° . The intensity of one peak is relatively high compared to the others in each deposition condition. This is due to having preferred crystal orientation, commonly found in WAAM [44]. The location of the peaks matches closely in each of the samples, indicating no significant peak shift in different heat input conditions. These XRD peaks are identified as the characteristic peak of pure Mo (JCPDS 42–1120) [7]. There is a peak at $2\theta \sim 27^\circ$ for all the samples shown as star mark in Fig. 8 which have been identified as the characteristic of molybdenum oxide (JCDPS 32–671) [45]. Characteristic peaks of carbide precipitates could not be found due to their low content. Danisman et al. [7] reported a similar result when they used spark plasma sintering to manufacture TZM. This issue was also found in the study of Azhar et al. [46] and they concluded that if the amount of phases is <1 wt%, the peaks could not be detected.

3.2. Mechanical property analysis

The microhardness tests were performed along the build direction on the four deposits, and the profiles are presented in Fig. 9. The hardness was measured from the substrate to the top of the deposit at a spacing of 0.5 mm. The average hardness of the 180A is 191.6 ± 7.6 hardness scale of Vickers (HV) with a minimum of 170.9 HV and a maximum of 205.2 HV. A standard deviation of 7.6 indicates that the data are close to the mean apart from some outliers. In the 200A, the average hardness is found 193.5 ± 6.5 HV, and the values range from 170.2 HV to 204.8 HV. The average hardness of the 220A and 240A are measured 192.5 ± 6.5 HV and 191.6 ± 7.6 HV, respectively. The hardness of the 220A ranges from 172.9 HV to 203.4 HV, while those of 240A range from 149.9 HV to 206.9 HV. Although the standard deviation is small, the range of the hardness is much higher due to drops and peaks in the values. This may be due to the microstructural heterogeneity in the structure.

Figure 10 compares the average microhardness among PM-TZM and the four WAAM deposits. PM-TZM has a comparatively higher hardness due to the finer grain size associated with the PM process. And, finegrain structure leads to higher hardness according to the Hall-Petch relationship. Lower hardness in WAAM-TZM could be attributed to larger grain size, which allows easier dislocation movement during the hardness test. Standard deviation is found to be the smallest in PM-TZM (5.4 HV), indicating the more homogenous microstructure. The average hardness of the deposits varies in close range from 188.5 HV to 193.5 HV, suggesting that variation of heat input condition has little effect on

the microhardness of the WAAM-TZM. This is because each deposit has similar microstructural features.

The tensile test result of the WAAM-TZM deposits is illustrated in Fig. 11. Tensile samples from each deposit were prepared along the build direction and tested at room temperature. Fig. 11 (a)-(d) shows the stress-strain curve of different heat input conditions. The result of the test is summarized in Fig. 11 (e)-(f) In 180A, the average ultimate tensile strength (UTS) is measured 29 \pm 7 MPa as shown in Fig. 11(e). The deformation of the 180A tensile samples is very low, <1% in each sample as indicated in Fig. 11(f). The average UTS of 200A condition is 192 ± 2.5 MPa with an average elongation of 1.28 \pm 0.08%. Both UTS and elongation are the largest in 200A condition among the four conditions. In the 220A condition, the average UTS is 83 \pm 1.83 MPa and elongation is 0.87 \pm 26%. For the 240A, two of the tensile samples broke during applying the preload (too brittle to test on this machine), and no significant data could be recorded. UTS and elongation were measured for a single sample and are found 50 MPa and 0.36% respectively. Lower strain in the samples (<2%) indicates that no significant plastic deformation occurred before fracture, and the samples went through brittle fracture during the test. In addition, there is no noticeable correlation between heat input conditions and mechanical property. Similar low elongation has been reported in other studies where unalloyed Mo has been fabricated by AM process. Rebesan et al. [47] reported elongation of 0.53% in LPBF of pure Mo and Wang et al. [48] reported elongation of 1.74% in WAAM of pure Mo. However, UTS was found >300 MPa at room temperature in both of the studies.

The macro-morphology of the fracture surfaces of the tensile specimens are flat and shiny, which represents brittle fracture. Fig. 12 represents the fractography images of the WAAM-TZM specimens. As the fracture mode is similar in all samples under the same heat input condition, SEM images of only one sample from each condition are shown in Fig. 12(a)-(l). Substantive pores in all fractured samples can be observed. Red marked areas show river-like patterns (chevron marks) at higher magnification. These marks indicate the fracture initiation point and the river-like pattern is the characteristic of transgranular brittle fracture. Blue marked areas show the presence of cracks and pores in the fracture surface at higher magnification. Transgranular brittle fracture is dominant in each case where cracks propagate across the grains. In addition, there is an absence of dimple-like features indicating the samples did not undergo any significant plastic deformation during the fracture. This is consistent with the tensile test result, in which elongation is very low. The presence of defects (e.g., pores and cracks) may have contributed to the brittle fracture of the tensile samples. This is because defects are the weakest point which can act as stress concentration sites during the tensile test. Due to the refractory alloy's intrinsic brittleness, cracks are propagated quickly after they are formed. Similar fracture characteristics are also reported by Wang et al. [48] in the study of WAAM Mo.

3.3. Porosity investigation

Figure 13 shows different types of pores generated during the WAAM process. They can be mainly classified according to their size as small spherical pores (SSPs) and in-homogeneously distributed large pores [33,39]. SSPs are defined as spherical pores with a volume <0.03 mm³ or equivalent to a diameter of 0.19 mm. Pores with a diameter larger than 0.19 mm are classified as large pores. Inverse pear-shaped pore (IPP) is also found where the top of the pore is larger than the bottom side, according to Wang et al. [32]. SSPs are found homogeneously distributed across the microstructure. IPP and large size pores are inhomogeneous in the structures. The lack of fusion pore is not observed in the microstructures. To quantitatively measure the porosity, ImageJ software was used [39].

Figure 14(a) shows the calculated porosity area fraction in four deposits. The 180A has a porosity area fraction of 1.599%. In the 200A, 220A, and 240A, the values are 1.0608%, 1.191%, and 2.042%,

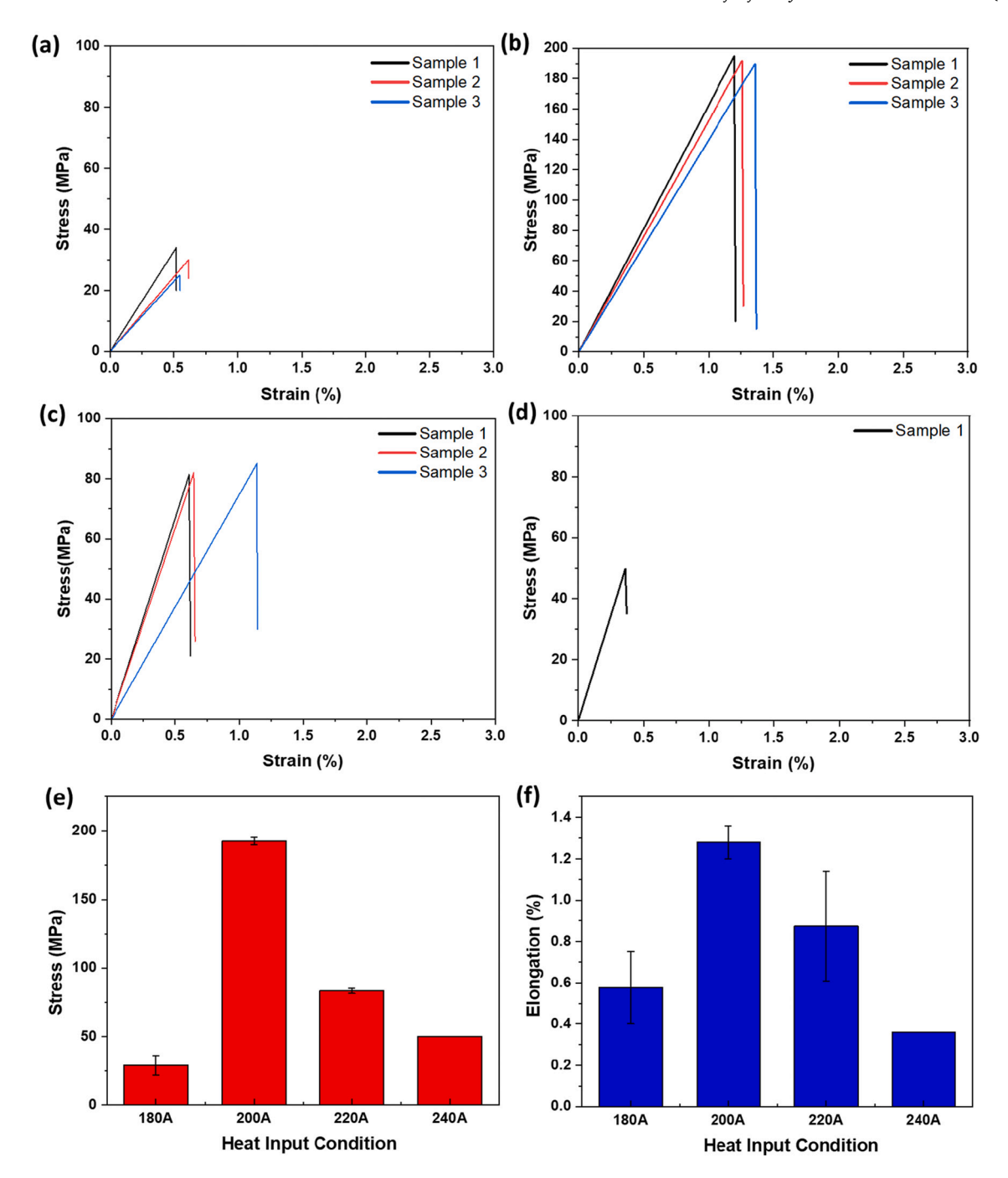


Fig. 11. Tensile test result of WAAM TZM deposits: (a) 180A, (b) 200A, (c) 220A, (d) 240A, (e) average ultimate tensile strength, and (f) average total elongation.

respectively. The 200A has the lowest fraction, while the 240A has the highest. Fig. 14(b) shows the relative frequency distribution of pore diameter for the different conditions. There is a sharp increase in the relative frequency of porosity up to 30 μm diameter in all conditions. >80% of the pores have a diameter lower than 30 μm . Relative frequency curves become flat when the diameter increases >100 μm . The major portion of the pore, approximately 98%, has a diameter of <190 μm , which is characterized as SSP. The relative frequency of large pores has been calculated at <2%, indicating their small effect on the total area fraction value.

4. Discussion

4.1. Correlation among process parameter, microstructure, and defects

During the solidification of the TZM, grain refinement is hindered due to the high solidification temperature, lack of lattice transformation in the BCC structure, and absence of solid-state phase transformation [23]. As a result from the WAAM process, coarse grains are formed, since it involves very high heat input and repeated melting of subsequently deposited layers [21]. In addition, the columnar structure is developed, due to the thermal cycles and high thermal gradients along the build direction. Similar microstructures are observed in WAAM of refractory metal [49], nickel-based superalloy [50], Ti-6Al-4 V [51,52], Steel [53], and high-entropy alloy [54]. From SEM images and EDS analysis in

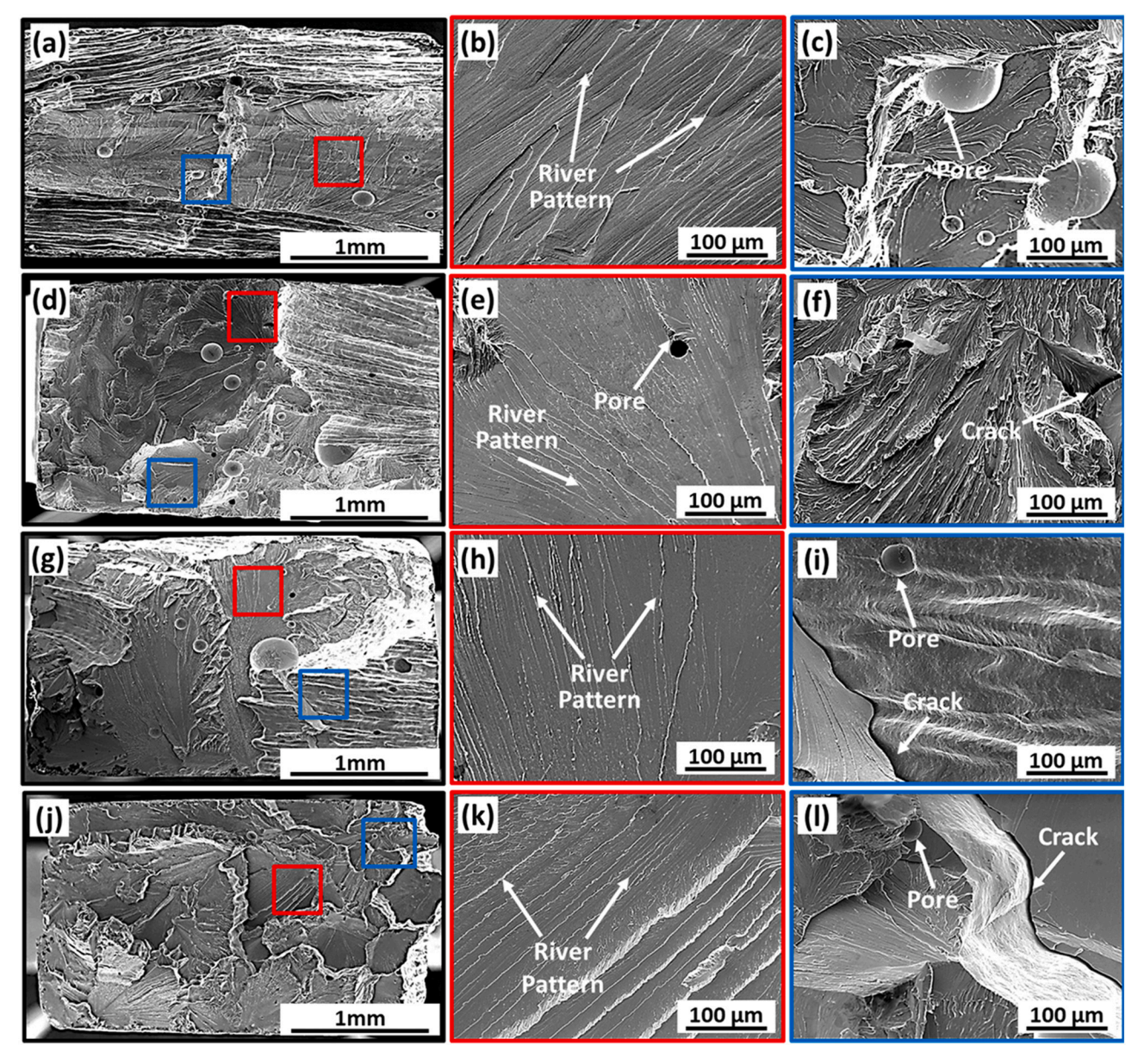


Fig. 12. SEM images showing fracture surfaces of WAAM-TZM tensile sample no. 1 at different magnification: (a-c)180A, (d-f) 200A, (g-i) 220A, and (j-l) 240A.

Fig. 6, small carbide precipitates, mainly TiC, are found homogeneously distributed in the microstructures. Similar types of carbide precipitates were found by Kaserer et al. in which TZM was deposited with LPBF [4]. In addition, these types of carbide precipitates are found in PM-TZM [7]. These carbide precipitates contribute to the increase in the recrystallization temperature of TZM alloy, compared to pure Mo.

In refractory alloys, oxygen plays a major factor in pore generation, since it can react to form oxides at high temperatures [5]. For example, Mo has a strong chemical affinity to oxygen and impurities at high temperatures, which can become a gas source. Pores can be easily generated during solidification at high temperatures during welding of TZM, according to Yang et al. [55]. This study uses an inert environment during the deposition, but oxygen could be embedded in the substrate and the wire. Consequently, the embedded oxygen is released and forms oxide at high temperatures during the WAAM process. The oxidation tendency of TZM alloy below 400 °C is comparatively low, but when the temperature reaches between 400 °C and 650 °C, there is an increasing probability of formation of MoOz (where z; $2 \leq z < 3$) oxide layers. When the temperature rises above 650 °C, the oxide layer becomes

 ${
m MoO_3}$ [5]. The boiling point of ${
m MoO_3}$ is 1155 °C, much lower compared to the melting point of TZM. As a result, during the welding process, ${
m MoO_3}$ can form easily in the presence of oxygen and generate pores if not removed completely during solidification. In addition, the Ti and Zr elements can also form oxides, which can lead to porosity if not eliminated during the deposition. Pores are also found in different studies during AM and welding of Mo and TZM. In a study conducted by Wang et al., SSP and IPP were found in WAAM-Mo [32]. Porosity was also found during the deposition of TZM by the LPBF process [4]. In addition, Chen et al. [33] performed EBW of pure Mo and found pore and cracks in the weld zone. The same results were also found in the research by Stutz et al. [56] during the EBW of TZM. In other studies, porosity was formed during the laser welding of Mo-alloy [57,58].

In this study, pores are characterized as SSPs, IPP, and large pores. A critical diameter value of 0.19 mm was selected for differentiating between the small and large pores [32]. IPP is a special-shaped large pore. The relative frequency of SSP is much higher compared to the large pore. During the deposition process, the metal is melted to form a molten pool, and a large number of SSPs are generated, as shown in Fig. 15(a). The

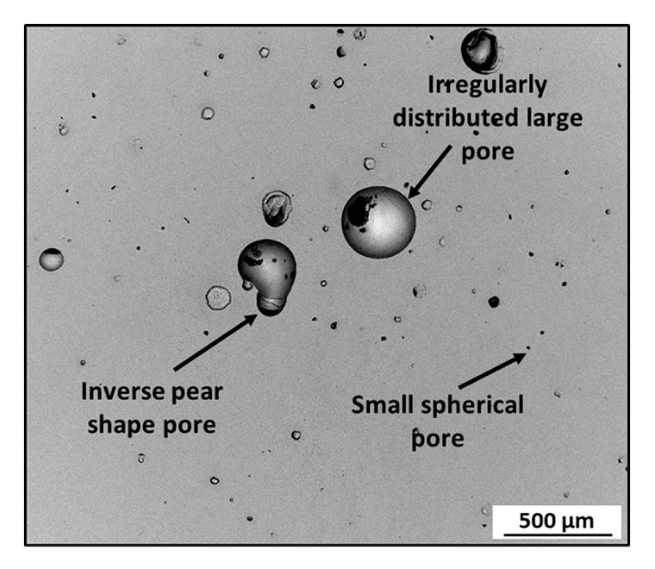


Fig. 13. SEM images show different pore types in WAAM-TZM: inverse pear-shaped pore (IPP), small spherical pore (SSP), and irregularly distributed large pore.

fluid flow in the molten pool is radially outward due to the Marangoni convection, and the pores in the molten pool move according to the fluid flow (Fig. 15(b)). Due to the small volume of SSPs, the buoyancy force acting upward direction is low. Therefore, they can't escape from the locations near the fusion boundary zone as this region is the first to solidify (Fig. 15(c)).

Consequently, SSPs are formed near the region of the fusion boundary [32]. When the next layer is deposited, some of the SSPs migrate in the molten pool, due to remelting of the previous layer [59]. There is a probability that they will merge and form a larger pore, as depicted in Fig. 15(d). During the deposition of another layer, SSPs in the remelted region will have the chance to be absorbed by the large pores and increase in the size (Fig. 15(e)). This phenomenon is repeated throughout the depositions, and the pores increase in the size. IPP can be formed when two large pores having different diameters come in contact at the layer interface and solidify without completely being merged due to the faster cooling at the layer interface. Due to the surface tension, the large pores remain spherical. The buoyancy force acting on the large pores is high which allows them to escape the molten pool during the

cooling process. Hence, the number of large pores is negligible compared to the SSPs. However, due to the high cooling rate of the WAAM process, some of these pores can not escape and solidify as large pores. If a slow cooling rate was conceivable, no significant large pore would occur, but the cooling rate is inherently high in the WAAM process. Fig. 14 shows that the porosity area fraction is the lowest for the 200A case and highest for the 240A. As heat input increases from 200A to 240A, more oxygen incorporates into the process zone and increases porosity. A similar result was found in a study by Ning et al. [1] when TZM alloy was welded using a fiber laser. Porosity area fraction increased with increasing the heat input. In Higashi and Ozaki, it was found that an energy density of at least 150 J/mm³ is needed to manufacture Mo samples with lower porosity [29]. In the 180A, energy density is 138 J/mm³, which is insufficient for removing pores from the melt pool. This contributed to the high porosity area fraction in the 180A compared to the 200A. A more in-depth investigation into the porosity formation mechanism will be performed in future studies using 3-dimensional computed tomography.

From the OM image in Fig. 4 and SEM images in Fig. 7, a small number of micro-cracks are present in the microstructures, but large networked cracks are not observed within the deposit. SEM images show that the cracks were generated from the side of the walls and propagated inside along the grains. They could be characterized as solidification cracks. Mo alloys are vulnerable to solidification cracking (hot cracking) because of the segregated oxygen impurities [4]. Due to the presence of MoO₃, the liquid film is formed during the crystallization process, which provides the conditions for the generation of solidification cracks. Similar cracks were found in the EBW of the Mo joint [33]. This type of cracking is dependent upon the solidification nature of the material and is caused by high strain on the melt pool or insufficient flow of liquid or flow obstruction by solidified grains [16]. Solidification cracking can also occur if very high energy is applied. Higher energy leads to higher thermal gradients, inducing larger thermal stress required for solidification cracking. This study used a high-intensity heat source for TZM deposition, which might have contributed to the crack formation. Residual stress plays a significant role in crack generation in the WAAM process. These cracks can act as stress generators under loading and result in poor mechanical properties of the structures. The authors will perform future studies regarding residual stress and crack mitigation for WAAM-TZM.

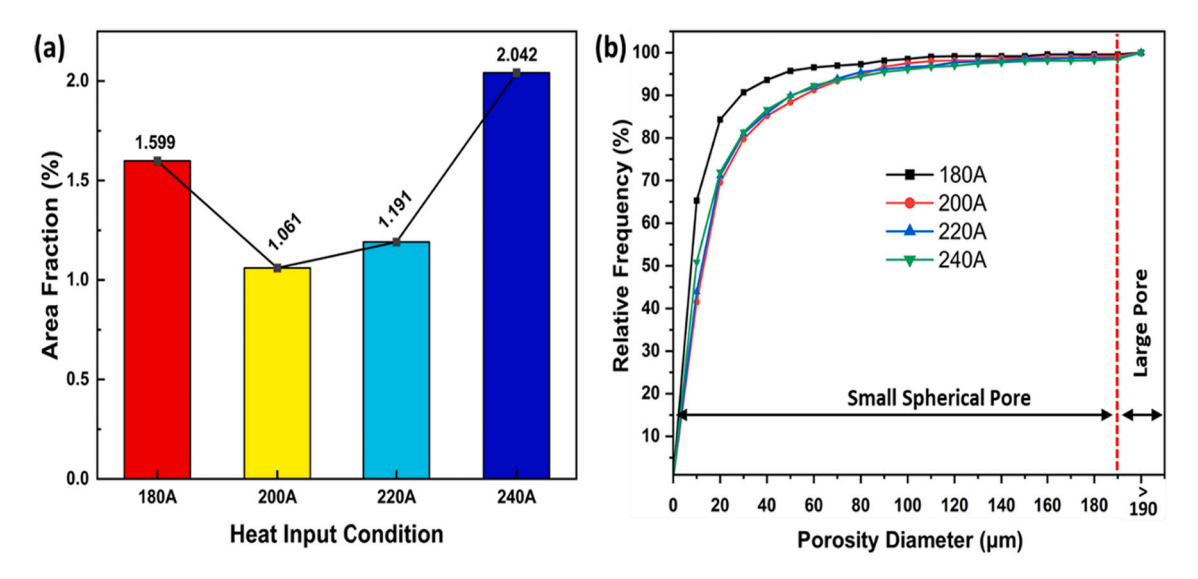


Fig. 14. (a) Porosity area fraction regarding different heat input conditions, (b) relative frequency distribution of porosity diameter for different heat input conditions.

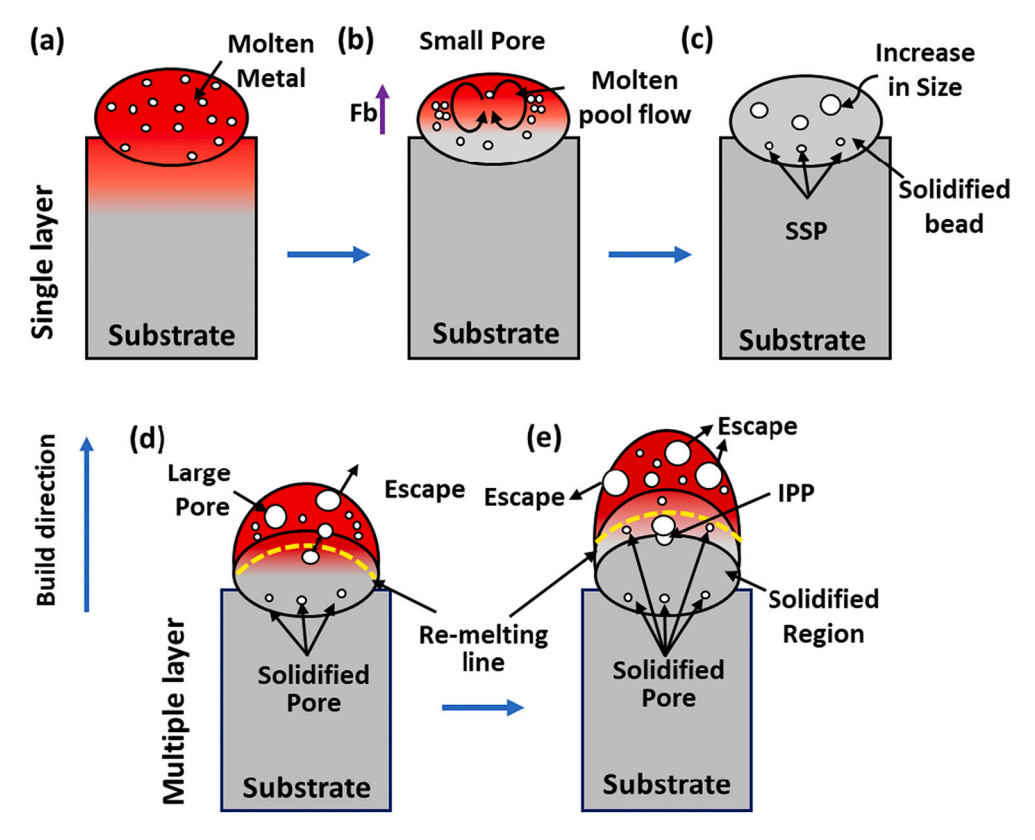


Fig. 15. Schematic diagram showing pore formation mechanism in WAAM-TZM.

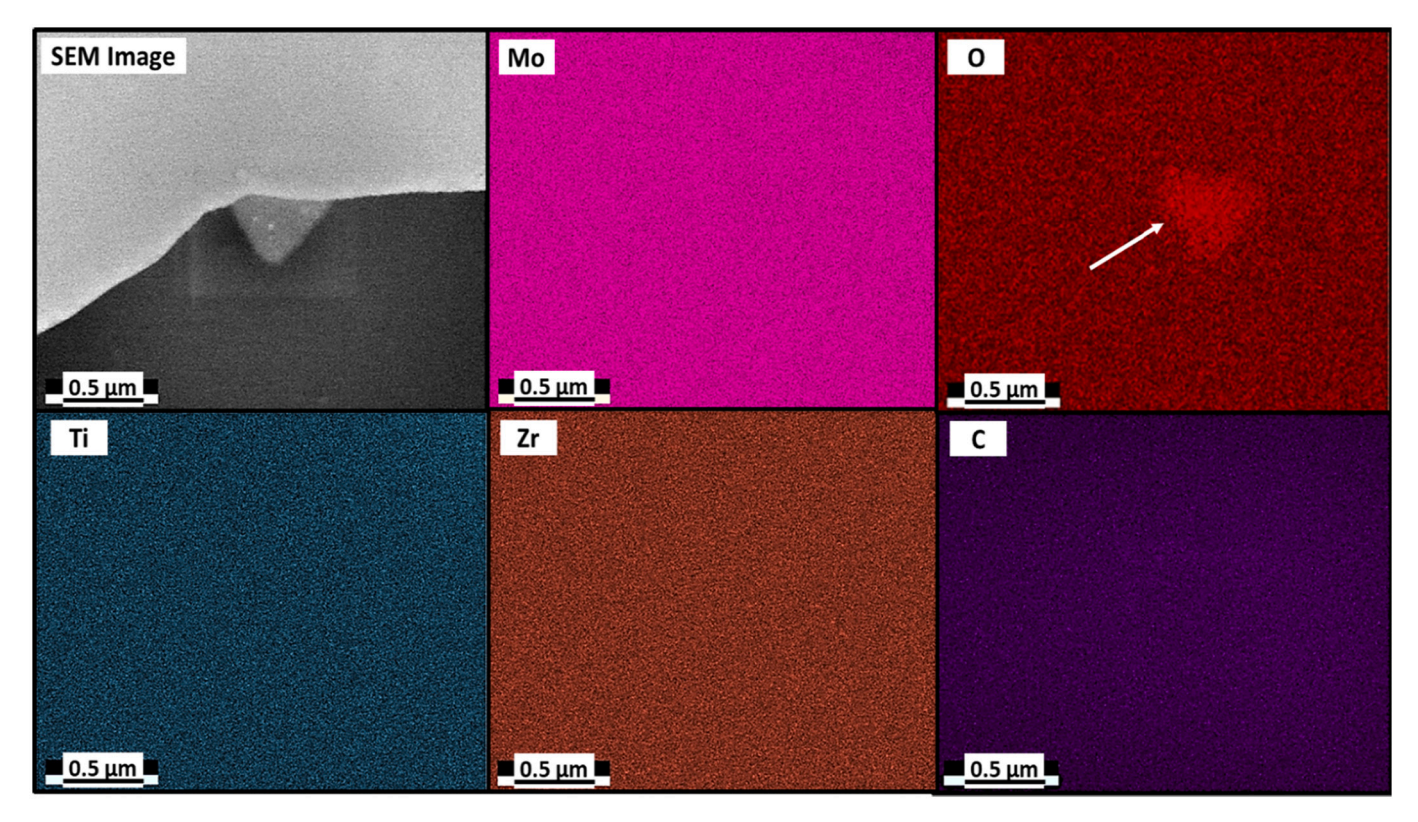


Fig. 16. SEM image and EDS analysis showing grain boundary oxides in the 180A WAAM-TZM.

4.2. Correlation among microstructure, defects, and mechanical properties

Coarse grain microstructure is typically characterized by lower hardness, toughness, and tensile properties [56]. Due to the increase of grain size, the strength of the material decreases because dislocation movement becomes easier as fewer grain boundaries are present. Grain boundaries act as an inhibitor to dislocation movement and increase strength. This phenomenon is explained by the Hall-Petch relationship, according to which the mechanical properties are dependent on grain size. In this study, coarse columnar grains are generated in WAAM-TZM. Due to the larger grain size, the average microhardness (i.e., ~190 HV) is lower compared to PM-TZM. In LPBF-TZM, the microhardness was 264 HV, and the increase in microhardness was attributed to the finer grain size [4]. The hardness value of the TZM joint was measured to be 300 HV in the weld zone and 220 HV in the heat-affected zone (HAZ) in the EBW process. During welding, fine grains are formed in the weld zone and coarse grains in HAZ, which contributed to a decrease in hardness value [60].

The tensile strength of the WAAM-TZM specimens is lower compared to the forged and rolled TZM alloys [61]. Among the tensile specimens, only two samples of the 200A condition have yield strengths of above 180 MPa. Elongation of the specimens is found to be <2% indicating insignificant plastic deformation before fracture and failure mode is brittle. Coarse grain size along with the defects are responsible for this poor mechanical property. This is supported by the study of Chen et al. in which the tensile strength of the Mo joint was reduced significantly due to the formation of coarse grain [33]. Porosity has been found as the major defect. It reduces the material strength because it can act as an initiation point of crack generation. It also decreases the part density, which contributes to the reduced mechanical property [37]. In the case of LPBF-TZM [4], no cracks were present and grain size was also smaller compared to the WAAM-TZM. However, the mean bending strength (267 MPa) was <50% compared to the PM case. Porosity in the structure (density 99.7%) contributed to the lower strength. Similarly, reduced mechanical strength is found in different studies of TZM welding. Stütz et al. found that the tensile strength of TZM welded specimens was only half of the base metal, and the fracture was mostly transgranular [56]. In Wang et al., the GTA-welded TZM joint had a tensile strength of 242 MPa with an elongation of 2% [35].

Grain boundary oxides are also one of the primary reasons for poor mechanical properties. It has been found that TZM welded joints are prone to embrittlement by even a small degree of grain boundary contamination from oxygen [23]. According to Kaserer et al., oxygen is soluble in molten Mo but almost insoluble in the solid form [4]. The residual oxygen-rich melt generates molybdenum oxide during solidification and solidifies along the grain boundary. To identify the presence of oxygen, EDS analysis was performed on WAAM-TZM components. Fig. 16 shows the EDS area map result from the middle part of the 180A deposits. The elemental analysis result shows a peak of oxygen at the grain boundary, indicating the presence of oxide particles in the structure. In addition, XRD results in Fig. 8 also confirm the presence of oxide particles in the structure. Oxygen impurity has also been found in other studies, especially in LPBF-TZM and welding of Mo alloys [4,23]. Grain boundary oxides may have contributed to the weakening of grain boundaries, and cracks could propagate easily during the application of load.

5. Conclusions

This study focuses on depositing TZM at different heat input conditions using the WAAM process and analyzes the relationships among process, microstructure, mechanical property, and defects. The following conclusion can be drawn from the study:

- Columnar grains are formed in all conditions, and the grains are elongated in the build direction. Carbide precipitates are found homogeneously distributed in the Mo matrix.
- Multi-scale pores are observed in the deposits, and they are characterized as SSP, IPP, and large pores based on size and shape. The highest porosity area fraction is calculated to be 2.04% in the 240A.
- The average microhardness value is evaluated 191.6 HV, 193.5 HV, 192.5 HV, and 188.5 HV in 180A, 200A, 220A, and 240A, respectively. The microhardness value is low compared to PM-TZM due to the formation of coarse elongated grain.
- \bullet The highest UTS is 192 MPa found in the 200A condition. Elongation of the tensile specimen is <2% in each heat input condition.
- Fractography images indicate that the fracture mode of the tensile specimen is mainly brittle transgranular. Porosity and river-like patterns are observed in the fracture surfaces. The EDS elemental analysis confirms the presence of oxygen impurities in the microstructures. These grain boundary oxides contribute to grain boundary weakening.
- Different defects (e.g., porosity, cracks, and grain boundary oxides) are present in the microstructures, deteriorating the mechanical property. To improve it, these defects should be minimized.

The mechanical properties of WAAM-TZM components are investigated in the build direction in this study. The results, however, may vary depending on the orientation of the specimens. The authors plan to expand on this research by examining the microstructures, deformation mechanisms, and anisotropic mechanical properties in greater detail. Residual stress development, mechanisms of porosity formation, and minimizing the number of pores will be studied in the near future.

Declaration of Competing Interest

The authors declare that they have no known competing financial interests or personal relationships that could have appeared to influence the work reported in this paper.

Data availability

Data will be made available on request.

Acknowledgements

The authors of this paper acknowledge the Center for Manufacturing Research (CMR) and Tennessee Technological University's Department of Manufacturing and Engineering Technology for their support. This material is based upon work supported by the National Science Foundation under Grant No. 2141905.

References

- J. Ning, K.M. Hong, G.V. Inamke, Y.C. Shin, L.J. Zhang, Analysis of microstructure and mechanical strength of lap joints of TZM alloy welded by a fiber laser, J. Manuf. Process. (2019), https://doi.org/10.1016/j.imapro.2019.02.015.
- [2] L. Kaserer, J. Braun, J. Stajkovic, K.H. Leitz, B. Tabernig, P. Singer, I. Letofsky-Papst, H. Kestler, G. Leichtfried, Fully dense and crack free molybdenum manufactured by selective laser melting through alloying with carbon, Int. J. Refract. Met. Hard Mater. 84 (June) (2019) 7, https://doi.org/10.1016/j.iirmhm.2019.105000.
- [3] G. Liu, G.J. Zhang, F. Jiang, X.D. Ding, Y.J. Sun, J. Sun, E. Ma, Nanostructured high-strength molybdenum alloys with unprecedented tensile ductility, Nat. Mater. 12 (4) (2013) 344–350. https://doi.org/10.1038/nmat3544.
- [4] L. Kaserer, J. Braun, J. Stajkovic, K.H. Leitz, P. Singer, I. Letofsky-Papst, H. Kestler, G. Leichtfried, Microstructure and mechanical properties of molybdenum-titanium-zirconium-carbon alloy TZM processed via laser powder-bed fusion, Int. J. Refract. Met. Hard Mater. (2020), https://doi.org/10.1016/j.ijrmhm.2020.105369.
- [5] B. Yavas, G. Goller, A novel approach to boriding of TZM by spark plasma sintering method, Int. J. Refract. Met. Hard Mater. (2019), https://doi.org/10.1016/j. ijrmhm.2018.10.006.
- [6] P. Hu, F. Yang, J. Deng, T. Chang, B. Hu, J. Tan, K. Wang, W. Cao, P. Feng, H. Yu, High temperature mechanical properties of TZM alloys under different lanthanum

- doping treatments, J. Alloys Compd. (2017), https://doi.org/10.1016/j.
- [7] C.B. Danisman, B. Yavas, O. Yucel, F. Sahin, G. Goller, Processing and characterization of spark plasma sintered TZM alloy, J. Alloys Compd. 685 (2016) 860–868, https://doi.org/10.1016/j.jallcom.2016.06.161.
- [8] K. Kılıçay, Development of protective MMC coating on TZM alloy for high temperature oxidation resistance by LPCS, Surf. Coat. Technol. (2020), https://doi. org/10.1016/j.surfcoat.2020.125777.
- [9] G. Moskal, A. Grabowski, A. Lisiecki, Laser remelting of silicide coatings on Mo and TZM alloy, Solid State Phenom. (2015), https://doi.org/10.4028/www.scientific. net/SSP.226.121.
- [10] S.P. Chakraborty, N. Krishnamurthy, Fabrication of a Mo based high temperature TZM alloy by non-consumable arc melting technique, in: Proc. - Int. Symp. Discharges Electr. Insul. Vacuum, ISDEIV, 2014, pp. 749–752, https://doi.org/ 10.1109/DFIV.2014.6961791.
- [11] I.G. Sharma, S.P. Chakraborty, A.K. Suri, Preparation of TZM alloy by aluminothermic smelting and its characterization, J. Alloys Compd. (2005), https://doi.org/10.1016/j.jallcom.2004.09.055.
- [12] M.A.M. Ghazali, M.A. Harimon, M.S. Mustapa, Mechanical behavior and microstructural analysis of molybdenum-TZM alloy subjected to different annealing temperature, JSE J. Sci. Eng. (2020), https://doi.org/10.30650/jse. v1i1 522
- [13] J. Fan, M. Lu, H. Cheng, J. Tian, B. Huang, Effect of alloying elements Ti, Zr on the property and microstructure of molybdenum, Int. J. Refract. Met. Hard Mater. (2009), https://doi.org/10.1016/j.ijrmhm.2008.03.006.
- [14] C.B. Danlşman, F. Şahin, O. Yücel, G. Göller, Microstructural Investigation of TZM Alloys Processed by Spark Plasma Sintering, 2016, https://doi.org/10.1557/ adv.2015.44
- [15] T. DebRoy, H.L. Wei, J.S. Zuback, T. Mukherjee, J.W. Elmer, J.O. Milewski, A. M. Beese, A. Wilson-Heid, A. De, W. Zhang, Additive manufacturing of metallic components process, structure and properties, Prog. Mater. Sci. 92 (2018) 112–224, https://doi.org/10.1016/j.pmatsci.2017.10.001.
- [16] S.W. Williams, F. Martina, A.C. Addison, J. Ding, G. Pardal, P. Colegrove, Wire + arc additive manufacturing, Mater. Sci. Technol. (United Kingdom) (2016), https://doi.org/10.1179/1743284715Y.0000000073.
- [17] O. Abdulhameed, A. Al-Ahmari, W. Ameen, S.H. Mian, Additive manufacturing: challenges, trends, and applications, Adv. Mech. Eng. (2019), https://doi.org/ 10.1177/1687814018822880.
- [18] ISO/ASTM 52900:2021(E), Additive manufacturing General principles Fundamentals and Vocabulary, 2021.
- [19] T.A. Rodrigues, V. Duarte, R.M. Miranda, T.G. Santos, J.P. Oliveira, Current status and perspectives on wire and arc additive manufacturing (WAAM), Materials (Basel). (2019), https://doi.org/10.3390/ma12071121.
- [20] J.L.Z. Li, M.R. Alkahari, N.A.B. Rosli, R. Hasan, M.N. Sudin, F.R. Ramli, Review of wire arc additive manufacturing for 3d metal printing, Int. J. Autom. Technol. (2019), https://doi.org/10.20965/ijat.2019.p0346.
- [21] B. Wu, Z. Pan, D. Ding, D. Cuiuri, H. Li, J. Xu, J. Norrish, A review of the wire arc additive manufacturing of metals: properties, defects and quality improvement, J. Manuf. Process. (2018), https://doi.org/10.1016/j.jmapro.2018.08.001.
- [22] J. Rodriguez, K. Hoefer, A. Haelsig, P. Mayr, Functionally graded SS 3161 to ni-based structures produced by 3D plasma metal deposition, Metals (Basel). (2019), https://doi.org/10.3390/met9060620.
- [23] A. Chatterjee, S. Kumar, R. Tewari, G.K. Dey, Welding of Mo-based alloy using electron beam and laser-GTAW hybrid welding techniques, Metall. Mater. Trans. A Phys. Metall. Mater. Sci. 47 (3) (2016) 1143–1152, https://doi.org/10.1007/ s11661-015-3267-8.
- [24] D. Jafari, T.H.J. Vaneker, I. Gibson, Wire and arc additive manufacturing: opportunities and challenges to control the quality and accuracy of manufactured parts, Mater. Des. (2021), https://doi.org/10.1016/j.matdes.2021.109471.
- [25] M. Khalil, G.H. Teichert, C. Alleman, N.M. Heckman, R.E. Jones, K. Garikipati, B. L. Boyce, Modeling strength and failure variability due to porosity in additively manufactured metals, Comput. Methods Appl. Mech. Eng. (2021), https://doi.org/10.1016/j.cma.2020.113471.
- [26] E. Ahmadi, M. Malekzadeh, S.K. Sadrnezhaad, Preparation of nanostructured high-temperature TZM alloy by mechanical alloying and sintering, Int. J. Refract. Met. Hard Mater. 29 (1) (2011) 141–145, https://doi.org/10.1016/j.iirmhm 2010.09.003
- [27] Y. Wei, L.M. Luo, X. Zan, J.P. Song, X.Y. Zhu, Y.C. Wu, Microstructural evolution and mechanical properties of carbon nanotubes–reinforced TZM composites synthesized by powder metallurgy, J. Alloys Compd. (2020), https://doi.org/ 10.1016/j.jallcom.2020.154540.
- [28] D. Faidel, D. Jonas, G. Natour, W. Behr, Investigation of the selective laser melting process with molybdenum powder, Addit. Manuf. 8 (2015) 88–94, https://doi.org/ 10.1016/j.addma.2015.09.002.
- [29] M. Higashi, T. Ozaki, Selective laser melting of pure molybdenum: evolution of defect and crystallographic texture with process parameters, Mater. Des. 191 (2020), https://doi.org/10.1016/j.matdes.2020.108588.
- [30] J. Braun, L. Kaserer, J. Stajkovic, K.H. Leitz, B. Tabernig, P. Singer, P. Leibenguth, C. Gspan, H. Kestler, G. Leichtfried, Molybdenum and tungsten manufactured by selective laser melting: analysis of defect structure and solidification mechanisms, Int. J. Refract. Met. Hard Mater. (2019), https://doi.org/10.1016/j. ijrmhm.2019.104999.
- [31] J. Braun, L. Kaserer, I. Letofsky-Papst, K.H. Leitz, H. Kestler, G. Leichtfried, On the role of carbon in molybdenum manufactured by laser powder bed fusion, Int. J. Refract. Met. Hard Mater. 92 (April) (2020) 5–10, https://doi.org/10.1016/j. iirmhm.2020.105283.

- [32] J. Wang, Y. Cui, C. Liu, Z. Li, Q. Wu, D. Fang, Understanding internal defects in Mo fabricated by wire arc additive manufacturing through 3D computed tomography, J. Alloys Compd. (2020), https://doi.org/10.1016/j.jallcom.2020.155753.
- [33] G. Chen, J. Liu, X. Shu, B. Zhang, J. Feng, Study on microstructure and performance of molybdenum joint welded by electron beam, Vacuum (2018), https://doi.org/10.1016/j.vacuum.2018.04.031.
- [34] Y. Zhang, T. Wang, S. Jiang, B. Zhang, Y. Wang, J. Feng, Effect of rhenium content on microstructures and mechanical properties of electron beam welded TZM alloy joints, J. Manuf. Process. 32 (2018) 337–343, https://doi.org/10.1016/j. imapro.2018.03.008.
- [35] H. Wang, Y. Zhang, X. Zhang, TZM alloy TIG welding process and microstructure of welded joints, Adv. Mater. Res. 291–294 (2011) 867–871, https://doi.org/ 10.4028/www.scientific.net/AMR.291-294.867.
- [36] M.R.U. Ahsan, G.-J. Seo, X. Fan, P.K. Liaw, S. Motaman, C. Haase, D.B. Kim, Effects of process parameters on bead shape, microstructure, and mechanical properties in wire + arc additive manufacturing of Al0.1CoCrFeNi high-entropy alloy, J. Manuf. Process. 68 (PA) (2021) 1314–1327, https://doi.org/10.1016/j. imapro.2021.06.047.
- [37] T. Hauser, R.T. Reisch, P.P. Breese, B.S. Lutz, M. Pantano, Y. Nalam, K. Bela, T. Kamps, J. Volpp, A.F.H. Kaplan, Porosity in wire arc additive manufacturing of aluminium alloys, Addit. Manuf. (2021), https://doi.org/10.1016/j.addma.2021.101993.
- [38] ASTM E8, ASTM E8/E8M standard test methods for tension testing of metallic materials 1, Annu. B. ASTM Stand. 4, no. C (2010) 1–27, https://doi.org/10.1520/F0008
- [39] Z.E. Tan, J.H.L. Pang, J. Kaminski, H. Pepin, Characterisation of porosity, density, and microstructure of directed energy deposited stainless steel AISI 316L, Addit. Manuf. 25 (Jan. 2019) 286–296, https://doi.org/10.1016/J.ADDMA.2018.11.014.
- [40] M.R.U. Ahsan, X. Fan, G.J. Seo, C. Ji, M. Noakes, A. Nycz, P.K. Liaw, D.B. Kim, Microstructures and mechanical behavior of the bimetallic additivelymanufactured structure (BAMS) of austenitic stainless steel and Inconel 625, J. Mater. Sci. Technol. (2021), https://doi.org/10.1016/j.jmst.2020.10.001.
- [41] Y. Kok, X.P. Tan, P. Wang, M.L.S. Nai, N.H. Loh, E. Liu, S.B. Tor, Anisotropy and heterogeneity of microstructure and mechanical properties in metal additive manufacturing: a critical review, Mater. Des. (2018), https://doi.org/10.1016/j. matdes.2017.11.021.
- [42] S. Thapliyal, Challenges associated with the wire arc additive manufacturing (WAAM) of aluminum alloys, Mater. Res. Express 6 (11) (Oct. 2019), 112006, https://doi.org/10.1088/2053-1591/AB4DD4.
- [43] G. Marinelli, F. Martina, S. Ganguly, S. Williams, Development of wire + arc additive manufacture for the production of large-scale unalloyed tungsten components, Int. J. Refract. Met. Hard Mater. 82 (February) (2019) 329–335, https://doi.org/10.1016/j.ijrmhm.2019.05.009.
 [44] S. Valkov, G. Kotlarski, M. Ormanova, N. Doynov, R. Ossenbring, P. Petrov,
- [44] S. Valkov, G. Kotlarski, M. Ormanova, N. Doynov, R. Ossenbring, P. Petrov, V. Michailov, Crystallography and mechanical properties of wire arc additively manufactured Al5356 components, Compt. Rend. L'Academie Bulg. des Sci. 74 (6) (2021) 820–827, https://doi.org/10.7546/CRABS.2021.06.03.
- [45] H. Hu, C. Deng, J. Xu, K. Zhang, M. Sun, Metastable h-MoO3 and stable α-MoO3 microstructures: controllable synthesis, growth mechanism and their enhanced photocatalytic activity, J. Exp. Nanosci. (2015), https://doi.org/10.1080/17458080.2015.1012654.
- [46] A.Z.A. Azhar, H. Mohamad, M.M. Ratnam, Z.A. Ahmad, The effects of MgO addition on microstructure, mechanical properties and wear performance of zirconia-toughened alumina cutting inserts, J. Alloys Compd. (2010), https://doi.org/10.1016/j.jallcom.2010.03.054.
- [47] P. Rebesan, M. Ballan, M. Bonesso, A. Campagnolo, S. Corradetti, R. Dima, C. Gennari, G.A. Longo, S. Mancin, M. Manzolaro, G. Meneghetti, A. Pepato, E. Visconti, M. Vedani, Pure molybdenum manufactured by laser powder bed fusion: thermal and mechanical characterization at room and high temperature, Addit. Manuf. 47 (Nov. 2021), 102277, https://doi.org/10.1016/J. ADDMA 2021 102277
- [48] J. Wang, C. Liu, T. Lu, R. Fu, T. Xu, Z. Li, C. Jing, Y. Cui, Microstructure and mechanical properties of unalloyed molybdenum fabricated via wire arc additive manufacturing, Int. J. Refract. Met. Hard Mater. 107 (Sep. 2022), 105886, https:// doi.org/10.1016/J.IJRMHM.2022.105886.
- [49] G. Marinelli, F. Martina, H. Lewtas, D. Hancock, S. Ganguly, S. Williams, Functionally graded structures of refractory metals by wire arc additive manufacturing, Sci. Technol. Weld. Join. (2019), https://doi.org/10.1080/ 13621718.2019.1586162.
- [50] A.N.M. Tanvir, M.R.U. Ahsan, G. Seo, J. Duk Kim, C. Ji, B. Bates, Y. Lee, D.B. Kim, Heat treatment effects on Inconel 625 components fabricated by wire + arc additively manufacturing (WAAM)—part 2: mechanical properties, Int. J. Adv. Manuf. Technol. (2020), https://doi.org/10.1007/s00170-020-05980-w.
- [51] J.R. Kennedy, A.E. Davis, A.E. Caballero, S. Williams, E.J. Pickering, P. B. Prangnell, The potential for grain refinement of wire-arc additive manufactured (WAAM) Ti-6Al-4V by ZrN and TiN inoculation, Addit. Manuf. 40 (February) (2021), 101928, https://doi.org/10.1016/j.addma.2021.101928.
- [52] G. Xian, J. Mok Oh, J. Lee, S.M. Cho, J.T. Yeom, Y. Choi, N. Kang, Effect of heat input on microstructure and mechanical property of wire-arc additive manufactured Ti-6Al-4V alloy, Weld. World 66 (5) (May 2022) 847–861, https:// doi.org/10.1007/S40194-021-01248-3.
- [53] P. Bajaj, A. Hariharan, A. Kini, P. Kürnsteiner, D. Raabe, E.A. Jägle, Steels in additive manufacturing: a review of their microstructure and properties, Mater. Sci. Eng. A (2020), https://doi.org/10.1016/j.msea.2019.138633.
- [54] Q. Shen, X. Kong, X. Chen, Fabrication of bulk Al-co-Cr-Fe-Ni high-entropy alloy using combined cable wire arc additive manufacturing (CCW-AAM):

- microstructure and mechanical properties, J. Mater. Sci. Technol. (2021), https://doi.org/10.1016/j.jmst.2020.10.037.
- [55] Z. Yang, K. Hu, D. Hu, C. Han, Y. Tong, X. Yang, F. Wei, J. Zhang, Y. Shen, J. Chen, X. Wu, Diffusion bonding between TZM alloy and WRe alloy by spark plasma sintering, J. Alloys Compd. 764 (Oct. 2018) 582–590, https://doi.org/10.1016/J. JALLCOM.2018.06.111.
- [56] M. Stütz, D. Oliveira, M. Rüttinger, N. Reheis, H. Kestler, N. Enzinger, Electron Beam Welding of TZM Sheets, 2017, https://doi.org/10.4028/www.scientific.net/ MSF.879.1865.
- [57] L.L. Zhang, L.J. Zhang, J. Long, X. Sun, J.X. Zhang, S.J. Na, Enhanced mechanical performance of fusion zone in laser beam welding joint of molybdenum alloy due to solid carburizing, Mater. Des. 181 (2019), https://doi.org/10.1016/j. matdes.2019.107957.
- [58] G. An, J. Sun, Y. Sun, W. Cao, Q. Zhu, Q. Bai, L. Zhang, Fiber laserwelding of fuel cladding and end plug made of La2O3 dispersion-strengthened molybdenum alloy, Materials (Basel). 11 (7) (2018), https://doi.org/10.3390/ma11071071.
- [59] L. Aucott, et al., Revealing internal flow behaviour in arc welding and additive manufacturing of metals, Nat. Commun. (2018), https://doi.org/10.1038/s41467-018.07900.0
- [60] Y. Zhang, T. Wang, S. Jiang, B. Zhang, Y. Wang, J. Feng, Microstructure evolution and embrittlement of electron beam welded TZM alloy joint, Mater. Sci. Eng. A (2017), https://doi.org/10.1016/j.msea.2017.05.076.
- [61] P. Hu, H. Li, Y. Gai Zuo, S. Wei Ge, S. Lei Li, H. Rui Xing, J. Yu Han, X. Jiang Hua, K. She Wang, L. Ping Li, Investigation of microstructure and tensile properties of asprocessed TZM alloy at elevated temperature, Mater. Charact. (2021), https://doi. org/10.1016/j.matchar.2021.110933.



Saiful Islam is a Ph.D. candidate in the Department of Mechanical Engineering at Tennessee Technological University. He obtained his B.Sc. degree in Industrial and Production Engineering from Bangladesh University of Engineering and Technology (BUET), Bangladesh. His research interest is in metal additive manufacturing, material characterization, and computational modeling.



Gijeong Seo is a Post-doctoral researcher in the Department of Manufacturing & Engineering Technology at Tennessee Technological University. He obtained his B·S. (2012), M. S. (2014), and Ph.D. (2019) from Pukyong National University, Korea. His research interest is in metal additive manufacturing, welding automation, and welding process development.



Md Rumman Ul Ahsan received his Ph.D. in Mechanical Engineering from Tennessee Technological University, USA. He obtained his Master's degree in advanced materials Engineering from Dong-Eui University, South Korea, and his bachelor's degree in Mechanical Engineering from Bangladesh University of Engineering and Technology (BUET), Bangladesh. His research interest is in metal additive manufacturing, welding, material characterization, and computational modeling.



Herminso Villarraga-Gómez is a Product Manager for X-ray Quality Solutions at ZEISS Industrial Quality Solutions. Herminso holds a PhD in Optical Science and Engineering at University of North Carolina at Charlotte. His current interests include contributing to the industry of quality control and advancing new manufacturing technologies such as additive manufacturing and new energy/battery materials.



Ho Jin Lee received his MS and PhD degrees at Chosun Univ., Republic of Korea, in 2014 and 2018. He has been a senior researcher in the Mechanical Components and Materials R&D Group, Korea Institute of Industrial Technology since 2018. His research interests include developing, applying, and simulation of a metal additive manufacturing process.



Duck Bong Kim received his MS and PhD degrees at Gwangju Institute of Science and Technology (GIST), Republic of Korea, in 2006 and 2011. He worked as a guest researcher at National Institute of Standards and Technology (NIST) from 2011 to 2016. He has been a professor in the Department of Manufacturing and Engineering Technology at Tennessee Technological University since 2016. His research interests include metal additive manufacturing, smart manufacturing, and data analytics.